



Cite this: *Chem. Sci.*, 2022, **13**, 6766

All publication charges for this article have been paid for by the Royal Society of Chemistry

Received 3rd April 2022  
 Accepted 23rd May 2022

DOI: 10.1039/d2sc01914k  
[rsc.li/chemical-science](http://rsc.li/chemical-science)

## 1. Introduction

Recently, lead halide perovskite materials have attracted great scientific interest for green energy applications.<sup>1,2</sup> In 1978, Weber reported the first organic–inorganic embodiment of this group, *i.e.*, methylammonium lead iodide,<sup>3</sup> which roots back to a report in 1893 by Wells about inorganic halide perovskites.<sup>4</sup> From 1980–90s, optical and electrical properties of three-dimensional (3D) and layered organic–inorganic, *i.e.*, two-dimensional (2D), metal halide perovskites were studied by Mitzi at IBM for mainly luminescence and transistor applications<sup>5–7</sup> and by others.<sup>8–10</sup>

In 2009, Miyasaka *et al.*<sup>11</sup> reported on the first perovskite solar cells (PSCs) impacting the photovoltaic research field significantly.<sup>12,13</sup> Within a few years, they compete with established technologies in terms of power conversion efficiency (PCE) with 25.7% in 2022 (ref. 14) while having additional benefits, *e.g.*, low-cost fabrication and higher efficiencies at lower light intensities. This successful emergence of this rather new class of solar cells relies on exceptional physical properties. Soon afterwards, they started to be investigated on other semiconductor applications such as lasers, detectors, scintillators, memories, and light-emitting diodes.<sup>15–18</sup>

However, all the mentioned successes are mainly achieved for lead-based perovskite compositions.<sup>19–21</sup> Unfortunately, the by-products of lead-based perovskites degradation are toxic and

could severely damage the environment ecosystem. This could be one of the major issues to developing perovskite research towards an industrialization level.<sup>22,23</sup> Therefore, developing less toxic perovskite compositions by replacing Pb is an important direction.

So far, various metal cations such as tin ( $\text{Sn}^{2+}$ ) or germanium ( $\text{Ge}^{2+}$ ) from group IVA (same group to  $\text{Pb}^{2+}$ ) and bismuth ( $\text{Bi}^{3+}$ ) or antimony ( $\text{Sb}^{3+}$ ) from the group VA have been explored as the alternatives for developing lead-free perovskites.<sup>24</sup> Moreover, a series of lanthanides,<sup>25</sup> alkaline metals,<sup>26</sup> partial replacement with different metals<sup>27</sup> as well as layered perovskites with double metal cites and general formulae  $\text{A}_2\text{BCX}_6$  (ref. 28) have been reported as well. However, to keep the crystal structure in the photoactive phase for the new perovskite compositions, the estimated tolerance factor based on the size and oxidation state of the atomic substituents from the empirical Goldschmidt rule<sup>29</sup> need to be considered. As a result, a bunch of new Pb-free perovskites with new possible applications have emerged. However, regarding the device application, especially in solar cell research, tin-based perovskites have been highly investigated due to their excellent physical properties, delivering the highest performance lead-free PSCs. Here, we present a perspective from the current status and prospects of tin-perovskites and the relevant devices, the benefits and drawbacks compared to other semiconductor device technologies, and especially compared to lead halide perovskite. Additionally, layered tin-based perovskite structures, single crystals and nanocrystals together with thin films have different properties and applications that are discussed in following sections.

<sup>a</sup>Institute for Photovoltaics (ipv), University of Stuttgart, Pfaffenwaldring 47, 70569 Stuttgart, Germany. E-mail: [mahdi.malekshahi@ipv.uni-stuttgart.de](mailto:mahdi.malekshahi@ipv.uni-stuttgart.de); [michael.saliba@ipv.uni-stuttgart.de](mailto:michael.saliba@ipv.uni-stuttgart.de)

<sup>b</sup>Helmholtz Young Investigator Group FRONTRUNNER, IEK5-Photovoltaik Forschungszentrum Jülich, 52425 Jülich, Germany



## 2. Tin-based perovskites

To understand the dependence of material properties on the atomic scale composition and further engineer the material for a wider range of applications, a new class of materials can be realized by metal replacement, *e.g.*, lead with other metals such as Sn or Ge.<sup>30</sup> On the other hand, the empirical tolerance factor defined from the cationic size of the metal needs to be between 0.8 and 1, and the oxidation state needs to be +2 for a stable cubic or tetragonal perovskite phase to form. However, the electronegativity of the metal and the halide can, in principle, determine the bandgap, effective mass, and lattice constant.<sup>26</sup> For many device applications, a visible light bandgap, low density of defect states and long diffusion lengths, and high charge mobilities are favourable. Thus, tin as an element from group IVA in the periodical table, same as lead, presents similar properties to lead, emerging as the most promising alternative candidate for lead.<sup>31</sup> Similar to lead-based perovskites, tin-based counterparts also show a noncubic phase at room temperature.<sup>32</sup> For example,  $\text{MASnI}_3$  crystallizes into a tetragonal phase with a space group of  $P4mm$  at room temperature. Unlike  $\text{FAPbI}_3$  with a non-perovskite yellow phase at room temperature, the  $\text{FASnI}_3$  remains in the black phase at different temperatures. In contrast, the cubic phase of  $\text{CsSnI}_3$  turns to the orthorhombic phase spontaneously. However, partial replacement of I by Br, *i.e.*,  $\text{CsSnI}_{3-x}\text{Br}_x$ , leads to transferring the orthorhombic to cubic crystal structure.<sup>33</sup> This section will overview different tin-based perovskites, focusing on their physical and chemical properties.

### 2.1. Fundamental properties

Sn and Pb, being in the same periodic group, have the same valence electrons configuration ( $ns^2np^2$ ).<sup>34</sup> Thus, tin-based perovskites show similar optoelectronic properties to lead-based counterparts, such as high charge carrier mobility, high light absorption properties, and small exciton binding energy.<sup>35</sup> These properties convert tin-based perovskites as suitable materials not only for solar cells but also for other

optoelectronic applications. However, tin differs in its fundamental atomic properties from lead. Unfortunately,  $\text{Sn}^{2+}$  quickly oxidizes to  $\text{Sn}^{4+}$  (eqn (1)) in the presence of oxygen (eqn (2)), which raises many challenges for the tin-based perovskite application.<sup>36,37</sup> Nevertheless, it has been reported that such oxidation even can occur in the absence of oxygen as well.<sup>38</sup>



The main reason for Sn oxidation has been identified as the absence of the lanthanide shrinkage effect, *i.e.*, Lorentz contraction for shells that are so far outside.<sup>39,40</sup> In the case of Pb, the two 6s electrons show inert activity and do not participate readily in chemical reactions (Fig. 1a). The lanthanide shrinkage effect in Pb refers to poor shielding of the nuclear charge by the 4f electrons, leading to drawing 6s electrons towards the nucleus and a smaller atomic radius.<sup>41</sup> As a result,  $\text{SnI}_2$  shows a higher Lewis acidity than  $\text{PbI}_2$ , leading to uncontrollable crystallization.<sup>34</sup>

On the other hand, as schematically shown in Fig. 1b, the Sn-5s in  $\text{MASnI}_3$  perovskite has higher energy levels and sharper conduction band minimum (CBM)-valence band maximum (VBM) edges than Pb-6s in  $\text{MAPbI}_3$ , leading to weaker Sn-I bonds due to reduced ionization energy.<sup>42</sup> This weak chemical bond in tin-based perovskites accelerates their reaction with  $\text{H}_2\text{O}$  and  $\text{O}_2$  molecules to form H-I and Sn-O bonds, which leads to faster oxidation.<sup>43</sup> Additionally, the Frost diagram illustrates the free Gibbs energy *versus* oxidation state of the elements is introduced to understand the relative stability of different oxidation states.<sup>44</sup> As shown in Fig. 1c, the  $\text{Pb}^{2+}$  indicates a deep asymmetric thermodynamic sink, demonstrating the stability of this oxidation state in Pb-based perovskites. While,  $\text{Sn}^{2+}$  shows a shallow thermodynamic sink in its Frost diagram, establishing an unstable oxidation state and leading to several unconventional oxidation pathways to higher and lower oxidation states, *i.e.*,  $\text{Sn}^{4+}$  and  $\text{Sn}^0$ .<sup>45,46</sup> Therefore,

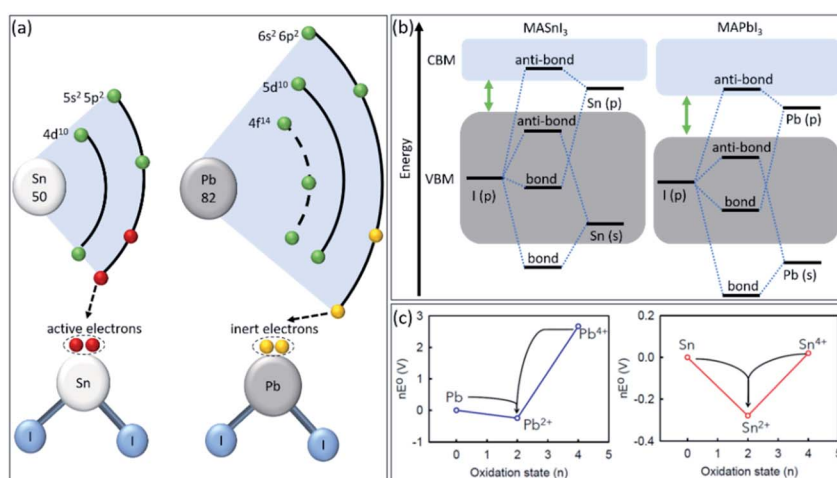


Fig. 1 (a) The electronic structure of Sn and Pb atoms. (b) Schematic energy levels of  $\text{MASnI}_3$  vs.  $\text{MAPbI}_3$  perovskites. (c) Frost diagrams of different oxidation states for Pb and Sn elements.<sup>47</sup> Copyright 2021, American Chemical Society.



introducing novel strategies to stabilize the  $\text{Sn}^{2+}$  oxidation state and change the shape of the Sn Frost diagram is crucial for achieving stable tin-based perovskite materials.

## 2.2. Thin films

Similar to lead-perovskites, fabricating high-quality perovskite films is essential to achieve high-performance tin-based

PSCs.<sup>35,48</sup> However, due to the higher Lewis acidity of  $\text{Sn}^{2+}$  compared to  $\text{Pb}^{2+}$ , *i.e.*, higher reactivity with other components in perovskite precursor, tin-based perovskites undergo faster and less controllable crystallization, which increases the number of pinholes in the final thin film.<sup>49</sup> Therefore, it is very crucial to develop new strategies to improve the uniformity and morphology of tin-based perovskite thin films.

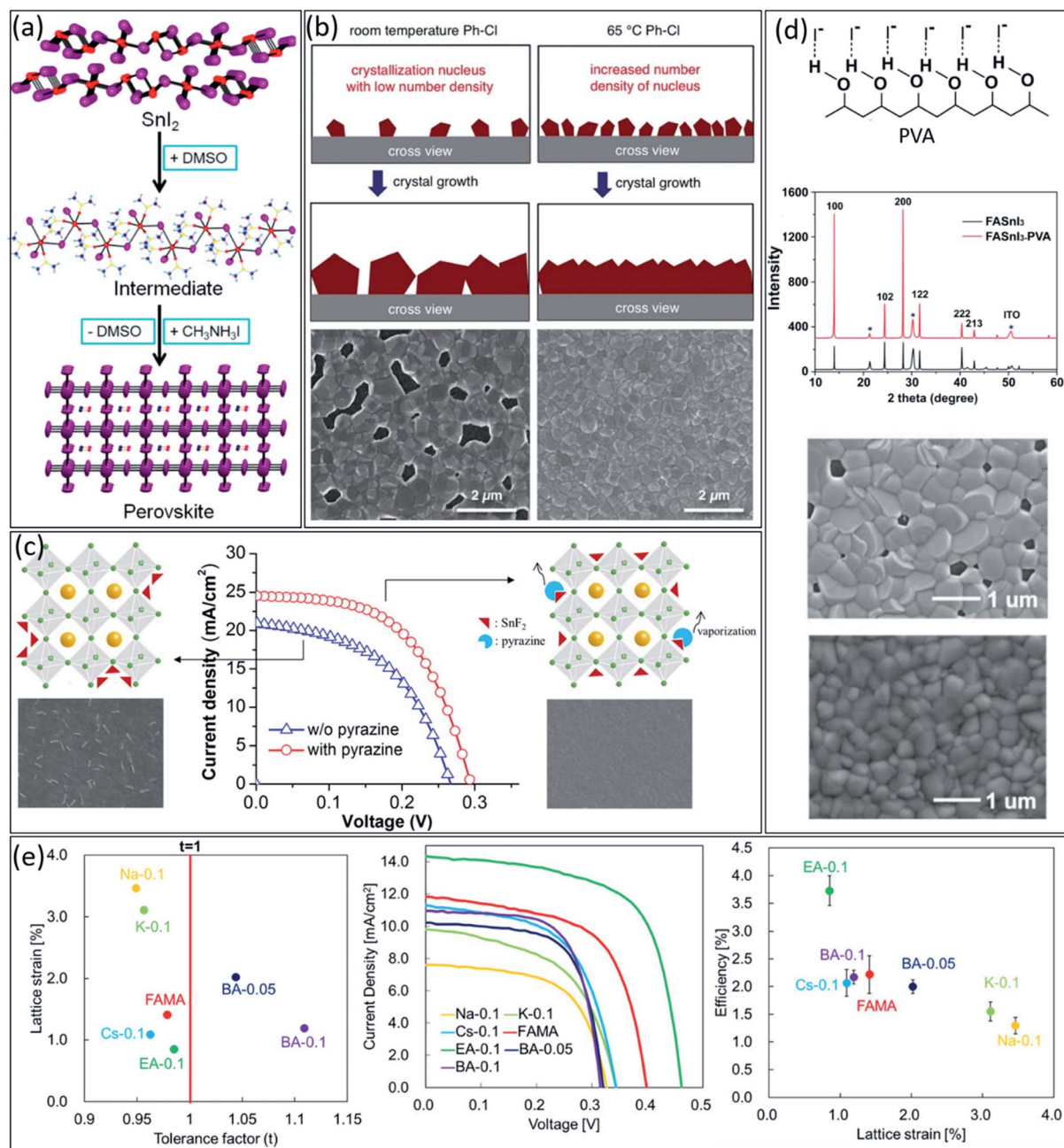


Fig. 2 (a) Schematic illustration of  $\text{SnI}_2\cdot3\text{DMSO}$  intermediate formation in tin-based perovskite.<sup>64</sup> Copyright 2015, American Chemical Society. (b) Schematic illustration of the effect of antisolvent temperature on the crystallization process and the corresponding SEM images of the resulting tin-based perovskite thin films.<sup>65</sup> Copyright 2018, Wiley. (c) Schematic illustrations, SEM images, and  $J$ – $V$  characteristics of  $\text{FASnI}_3$  thin films in the absence and presence of pyrazine.<sup>59</sup> Copyright 2016, American Chemical Society. (d) Schematic illustration of the  $\text{O}-\text{H}\cdots\text{I}^-$  hydrogen bonding interaction between PVA and iodide atoms, XRD patterns, and SEM images of  $\text{FASnI}_3$  and  $\text{FASnI}_3$ -PVA perovskite films.<sup>66</sup> Copyright 2019, Wiley. (e) Relationship between the lattice strain, the tolerance factor ( $t$ ) and achieved efficiencies for various cation-substituted in tin-based perovskites.<sup>63</sup> Copyright 2019, American Chemical Society.



Generally, it is challenging to fabricate pinhole-free perovskite thin films with pure dimethylformamide (DMF) as the solvent of perovskite precursors due to the lack of a stable intermediate phase between nucleation and growth steps during crystallization. Solvent engineering has been introduced for stabilizing the intermediate phase, resulting in more controllable crystallization.<sup>50</sup> Similar to lead-based perovskite, dimethyl sulfoxide (DMSO) makes a strong Lewis acid–base adduct with  $\text{Sn}^{2+}$  element. It provides a stable transitional  $\text{SnI}_2 \cdot 3\text{DMSO}$  intermediate phase, leading to more homogeneous nucleation and crystallization (Fig. 2a).<sup>51</sup> Therefore, using DMSO as the main or co-solvent for the preparation of tin-based precursor solution is essential. However, recently, it has been demonstrated that DMSO itself could undergo some chemical reaction over 100 °C during the perovskite precursor preparation due to the high reactivity of  $\text{Sn}^{2+}$ , producing dimethylsulfide (DMS) and  $\text{Sn}^{4+}$  byproducts.<sup>38</sup>

Besides the solvent of the precursors, antisolvent also plays a crucial role in the quality of tin-based perovskite films. An ideal antisolvent needs to be able to balance the nucleation and crystal growth processes during the film crystallization.<sup>52,53</sup> So far, chlorobenzene (CB) has shown the best performance among various antisolvents, providing highly crystalline thin films with excellent morphology after treating the wet tin-based perovskite precursor during the spin coating step.<sup>54</sup> Since the temperature of antisolvents can affect their miscibility properties; therefore this parameter also must be taken into account.<sup>55</sup> As shown in Fig. 2b, the hot CB as antisolvent, *i.e.*, 65 °C temperature, can increase the density of nucleation sites compared to room temperature CB, which leads to higher quality tin-based perovskite thin film.<sup>56</sup>

Additives engineering is another efficient approach to controlling the morphology and quality of tin-based perovskite thin films. Generally, an ideal additive, depending on its functional group, should have an effective chemical interaction with perovskite components to improve the quality of thin films.<sup>57,58</sup> Firstly, pyrazine was added to tin-based perovskite precursor as a co-additive with  $\text{SnF}_2$  to suppress the  $\text{Sn}^{2+}$  oxidation and homogeneous dispersion of  $\text{SnF}_2$  in the thin film by forming the  $\text{SnF}_2$ –pyrazine complex.<sup>59</sup> The  $\text{SnF}_2$ –pyrazine complex forms by strong  $\text{d} \rightarrow \pi^*$  back-donation coordination from tin(II) halide to the pyrazine ring. As shown in Fig. 2c, the existence of this complex in the perovskite composition leads to a dense thin film without any phase separation, suppressing the trap states and improving the device performance. As another example, as shown in Fig. 2d, poly(vinyl alcohol) (PVA) molecules exhibit a hydrogen bonding interaction with the iodide ions in  $\text{FASnI}_3$  perovskite precursor, leading to slow down the crystal growth process and homogeneous perovskite thin films, consequently. Similarly, polymethyl methacrylate (PMMA) as an additive could improve the  $\text{FASnI}_3$  quality by interacting the carbonyl group in PMMA structure with the  $\text{Sn}^{2+}$  cations in perovskite precursor.<sup>60,61</sup>

Additionally, lattice strain engineering is another approach to controlling the quality of tin-based perovskite thin films. The lattice strains in the perovskite structure scatter the carrier diffusion and create the charge recombination centres in

perovskite films.<sup>62</sup> Therefore, developing efficient strategies to suppress the strains in perovskite lattice is crucial for achieving high-efficiency tin-based PSCs. In this regard, Nishimura *et al.* studied the relationship between lattice strain in tin-based perovskite film and the efficiency of fabricated PSCs.<sup>63</sup> They prepared tin-based  $\text{Q}_x(\text{FA}_{0.75}\text{MA}_{0.25})_{1-x}\text{SnI}_3$  perovskites, where Q was various cations with different ionic radius such as  $\text{Na}^+$ ,  $\text{K}^+$ ,  $\text{Cs}^+$ , ethylammonium ( $\text{EA}^+$ ), and butylammonium ( $\text{BA}^+$ ). Firstly, they compared the relationship between the lattice strain and the tolerance factor ( $t$ ) for different perovskite compositions. Interestingly, they demonstrated an inverse relationship between the lattice strain and  $t$  (Fig. 2e). Among different cations, EA-perovskite film showed the minimum lattice strain of 0.85 with a closer  $t$  to 1, leading to the highest carrier mobility of  $43.03 \text{ cm}^{-2} \text{ V s}$ . As shown in Fig. 2e, they observed a good correlation between efficiency and the lattice strain for different tin-based perovskite films, achieving the highest PCE for EA-PSC with the lowest lattice strain among all Q cations. These results suggest that controlling the lattice strain of tin-based perovskites could suppress the charge carrier trapping sites, leading to improved photovoltaic parameters such as  $V_{oc}$ ,  $J_{sc}$ , and FF.

In summary, solvent, additive and lattice strain engineering can be considered as efficient approaches to control the nucleation and growth process during tin-based perovskite crystallization, leading to high-quality thin films.

### 2.3. Layered structures

Layered structures, *i.e.*, 2-dimensional (2D) perovskites, are considered as a new class of perovskite materials. Generally, in 2D perovskites, a long-chain organic monovalent cation by which the typical cubic/tetragonal perovskite structure transforms to a layered orthorhombic perovskite.<sup>67,68</sup> These structures can further show different dimensionalities ( $n = 2$  till  $\infty$ ) by having different stackings of methylammonium and long organic molecule chains, constructing 3D/2D structures (Fig. 3a). These materials exhibit better stability against degradation and have directional dependence physical properties. Here, tuneable excitonic properties, light-absorbing, and electronic characteristics<sup>69</sup> by engineering the dimensionality are feasible. The layered structure can suppress the self-doping assisted degradations and the oxidation of  $\text{Sn}^{2+}$  in these materials. The same approaches for engineering the material processing of 3D perovskites have been followed to make layered tin-based perovskites even more stable. With different stacking orders and long-chain organics, the perovskite dimension can be optimized towards both stability and high performance.<sup>70</sup> Even defect engineering<sup>71</sup> and doping of bulk, and 2D perovskite can enhance the performance of tin-based solar cells.<sup>72</sup> Quantum confinement effects exist in lower dimensions due to the spatial restriction for charge carriers; however, the absorption coefficient is typically lower than the 3D bulk perovskite structures due to the lower number density of light-absorbing centres (here metal and halide). Firstly, Mitzi *et al.* reported the synthesis of a family of organic-based layered tin-based perovskites,  $(\text{C}_4\text{H}_9\text{NH}_3)_2(\text{CH}_3\text{NH}_3)_{n-1}\text{Sn}_n\text{I}_{3n+1}$ , which



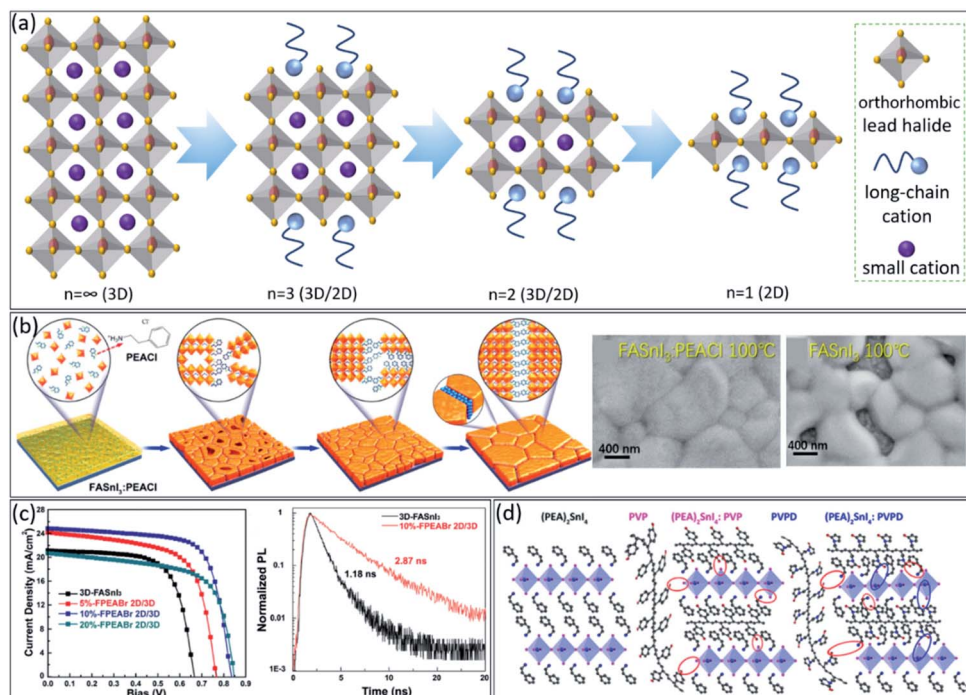


Fig. 3 (a) Schematic illustration of constructing different dimensionalities of perovskite ( $n = \infty$  till 1) with varying stackings of methylammonium and long-chain organic cations. (b) Schematic illustration of tin-based perovskite crystal change in the presence of PEACl as the long-chain cation during temperature annealing processes and the corresponding SEM images.<sup>74</sup> Copyright 2020, American Chemical Society. (c) J-V curves of fabricated PSCs with pure 3D FASnI<sub>3</sub> and 2D/3D perovskite with different FPEABr concentrations, as well as, the TRPL spectra of the pure FASnI<sub>3</sub> and 10%-FPEABr (the best concentration) perovskite films.<sup>75</sup> Copyright 2021, Wiley. (d) Schematic illustrations of the interactions between the PVP and PVPD polymers chains.<sup>77</sup> Copyright 2021, American Chemical Society.

show a similar transition from semiconducting to metallic behaviour with increasing the  $n$ .<sup>73</sup>

Regarding the layered structure in bulk, our group demonstrated that phenyl ethylammonium chloride (PEACl) helps to grow higher members of 2D crystals into the 3D tin-based perovskite matrix with excellent vertical crystal orientation and grain sizes up to 1  $\mu\text{m}$  (Fig. 3b).<sup>74</sup> As a result, the FASnI<sub>3</sub>-PEACl device showed a PCE of 9.1% with negligible hysteresis and noteworthy stability over 1500 h under storage in the dark condition. Interestingly, the best record PCE of tin-based PSCs was achieved by 3D/2D perovskite structure.<sup>75</sup> As shown in Fig. 3c, the pure FASnI<sub>3</sub>-based device obtained PCE of 9.38%, while inducing FPEABr up to 10% into perovskite film leads to achieving the highest PCE of 14.8%. The prominent role of this 3D/2D microstructure was mentioned as suppressing the well-known oxidation from Sn<sup>2+</sup> to Sn<sup>4+</sup> and decreasing defect density (see the TRPL data in Fig. 3c).

The 2D monolayers are another class of materials with idiosyncratic characteristics compared to bulk and thin-film materials.<sup>76</sup> They have a unique potential for new generation optoelectronics and photonics. Broken symmetry due to the layered structure, special magnetic responses with enhanced Rashba tension-based engineering, and more susceptibility for large lattice deformations due to external stimuli, new physics, and tunable properties are among the unique topics related to this class of materials. And most recently, the perovskite 2D monolayers have been predicted and investigated in several

publications.<sup>76</sup> Typical thicknesses are a few nanometres. For instance, PEA<sub>2</sub>SnI<sub>4</sub>,<sup>77</sup> with a preferred directional charge transport and a suppressed ion migration has been implemented in field-effect transistors, improving the device performance. As schematically shown in Fig. 3d, poly(vinyl alcohol) (PVP) and poly(vinyl pyrrolidone) PVPD chains fill into the perovskite grain boundaries during the crystallization of the (PEA)<sub>2</sub>SnI<sub>4</sub> films, thereby improving the surface morphology and reducing the roughness of the films, *i.e.*, 2D layered structure. Moreover, this 2D layered structure suppresses the tin oxidation in the air by creating the secondary bonds between the polymers and (PEA)<sub>2</sub>SnI<sub>4</sub>. However, preparing a well-tuned 2D layered hierarchical on top of 3D tin-based perovskite films is very challenging to suppress the Sn<sup>2+</sup> oxidation and improve the film stability efficiently. That is why still many research groups focusing on this topic vastly.<sup>78–80</sup> For example, recently, Xu *et al.* demonstrated that using ammonium chloride (NH<sub>4</sub>Cl) as the additive is necessary to control the orientation of the 2D layered structure onto 3D tin-based perovskite.<sup>81</sup> They confirmed that the pure AVA<sub>2</sub>FA<sub>n</sub>Sn<sub>1</sub>I<sub>3n+1</sub> ( $n = 5$ ) (AVA = 5-ammonium valeric acid) shows a random 2D orientation; however, by using 5% NH<sub>4</sub>Cl additive, the perovskite film indicates a preferential vertical orientation, which is favourable for charge transport between two electrodes, leading to improve the uniformity and morphology of the perovskite film.

In summary, 2D tin-based perovskites could be prepared by introducing long-chain cations in perovskite crystals. These

long-chain cations could suppress tin oxidation and improve film stability. However, the poor conductivity of these long chains cations in pure 2D structures may confine the charge transfer properties of perovskite film, therefore, combining this structure into the bulk or as a monolayer on the surface of 3D perovskite, *i.e.*, 3D/2D structures, could be a promising direction to enhance the stability and photovoltaic performance of tin-based PSCs, simultaneously.

#### 2.4. Nanocrystals and single crystals

After discovering the lead-based perovskite nanocrystals (NCs) in 2014, they have shown significant advances in recent years.<sup>82–84</sup> However, similar to other perovskite structures, substituting lead with less toxic elements must be considered for future commercial development. Due to the comparable ionic radius of  $\text{Sn}^{2+}$  and  $\text{Pb}^{2+}$ , Sn could replace in the perovskite lattice without disturbing the crystal structure. Tin-based perovskite NCs have shown attractive advantages similar to thin films.<sup>85</sup> So far, they have been utilized for high-efficiency solar cells, sensors, LEDs, and medical imaging devices.<sup>86</sup> However, their synthesis process is more complicated than lead-based NCs due to the unstable oxidation states of tin. The most common strategies to improve the stability of tin-based NCs include ligand functionalization, doping, alloying and core-shell structures.<sup>87</sup> To date, hot-injection, ligand-assisted reprecipitation, chemical vapor deposition, and solvothermal

reaction have been used extensively to synthesize high-quality colloidal NCs with controlled morphologies and sizes for achieving near-perfect optical/photophysical properties.<sup>88</sup>

Firstly, in 2016, Jellicoe *et al.* synthesized  $\text{CsSnX}_3$  (X = Cl, Br, I) NCs, exploring their spectral tunability through quantum confinement effects and control of the anionic composition.<sup>89</sup> They demonstrated that the bandgap could be tuned from the visible to the near-IR region by changing the halides from chloride to bromide (Fig. 4a). Moreover, similar to the bulk perovskite, this red-shifted in tin-based NCs compared to lead-based analogous was explained due to higher electronegativity of the tin in the 'B' site of  $\text{ABX}_3$  structure.<sup>90</sup>

Unfortunately, most colloidal tin-based NCs tend to precipitation over time, up to two weeks, due to the dynamic character of ligand absorption and desorption processes.<sup>91</sup> Moreover, once tin-based NCs exposed to ambient conditions,  $\text{Sn}^{2+}$  quickly turned to  $\text{Sn}^{4+}$ , leading to decomposition of NCs. Similar to bulk tin-based perovskite, synthesis of the 2D layered structures could enhance the stability of NCs against oxygen and humidity owing to the surface passivation by ligands.<sup>34,92</sup> As shown in Fig. 4b, 2D perovskite NCs, *i.e.*, nanoplatelets, could be synthesized with general  $\text{L}_2[\text{ABX}_3]_{n-1}\text{BX}_4$  formula, where A is a cation, B is a metal, X is a halide, and L is a long-chain ligand.<sup>93</sup> In this structure, the L limits growth in one dimension and improve the stability of NCs. The thickness of the nanoplatelets is defined as  $n - 1$  term in the general 2D structure formula. The  $n = 2$  and  $n = 1$  present a complete unit cell

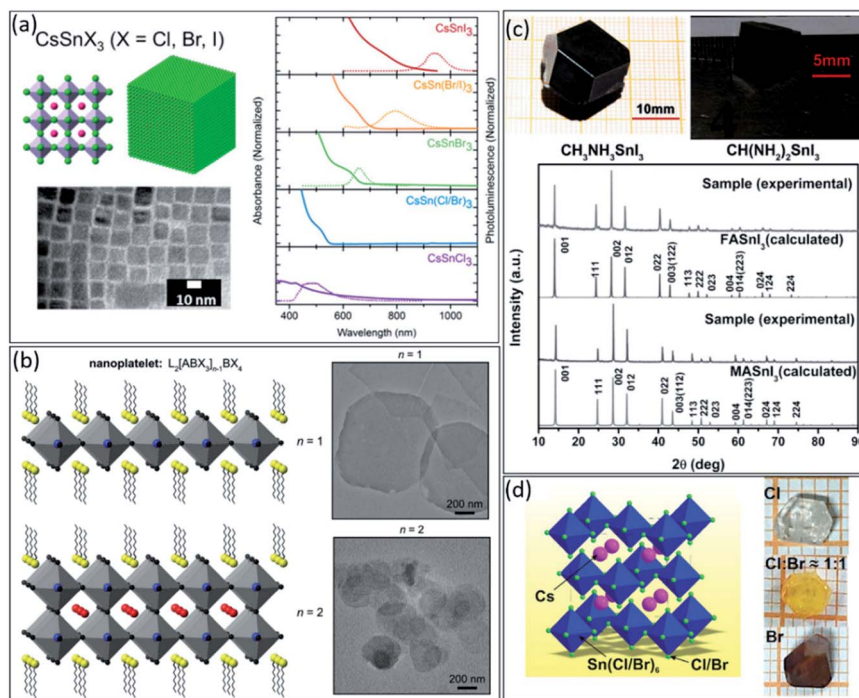


Fig. 4 (a) The schematic illustration, TEM image, absorbance, and steady-state PL  $\text{CsSnX}_3$  (X = Cl, Br, I) perovskite nanocrystals.<sup>89</sup> Copyright 2016, American Chemical Society. (b) The schematic illustration and the corresponding TEM images of the perovskite nanoplatelets with thicknesses  $n = 1$  and  $n = 2$ .<sup>93</sup> Copyright 2016, American Chemical Society. (c) The photographs and XRD patterns of obtained  $\text{MASnI}_3$  and  $\text{FASnI}_3$  single crystals by optimizing crystal growth conditions.<sup>99</sup> Copyright 2016, Wiley. (d) The 3D crystal structure illustration of the  $\text{Cs}_2\text{SnCl}_{6-x}\text{Br}_x$  perovskites and photographs of single-halide and mixed-halide  $\text{Cs}_2\text{SnCl}_{6-x}\text{Br}_x$  single crystals with body colours changing from transparent to yellow and finally to dark red.<sup>100</sup> Copyright 2019, Wiley.



and layered structure, an incomplete unit cell that lacks the A cation (see the schematic and TEM images in Fig. 4b). Tisdale *et al.*<sup>94</sup> demonstrated that the absence of A cation in a layered structure, *i.e.*,  $n = 1$ , has a negligible effect on the NCs absorption and emission energy. However, by decreasing the  $n$  values from 2 to 1, photoluminescence quantum yield (PLQY) would also decrease, which is expected due to reduced nanoplate thicknesses. Therefore, without disturbing the optical characteristic of tin-based NCs, it is possible to improve their stability by decreasing the dimension from 3D to 2D. Every long-chain cation with a proper functional group to coordinate with the perovskite component, *i.e.*,  $\text{Sn}^{2+}$  or  $\text{NH}_3^+$ , could be used for this purpose.<sup>57,58,94,95</sup>

Generally, most of the instabilities issues of perovskite materials are directly related to morphological disorder at grain boundaries and surface degradation.<sup>96</sup> In contrast, perovskite materials in the single-crystalline form exhibit no grain boundaries and possess low trap densities; and are likely to show superior optoelectronic performances and better stability compared to their polycrystalline film counterparts.<sup>97</sup> Due to the narrow bandgap properties of tin-based perovskites, their single crystals are most likely suitable to emit pure red light and near-infrared light, so they may further be the best candidates for optical display or diagnostic applications.<sup>98</sup>

However, growing the tin-based single crystals under an ambient atmosphere is challenging due to the tin instability. Firstly, Dang *et al.*<sup>99</sup> synthesized  $\text{MASnI}_3$  and  $\text{FASnI}_3$  single crystals utilizing a top-seeded solution growth method under ambient conditions (Fig. 4c). In this method, controlling the growth temperature and selecting the high-quality seed crystal is essential to achieving the high-quality single crystal. As shown in Fig. 4c, the XRD diffraction patterns of the single crystals were well-matched with the calculated patterns without presenting any impurities. This study provides new information about the fundamental properties of  $\text{MASnI}_3$  and  $\text{FASnI}_3$  single crystals and potentially guides solar cell applications, field-effect transistors (FETs), and thermoelectric devices.

Different from  $\text{FASnI}_3$  and  $\text{MASnI}_3$  with a  $Pm\bar{3}m$  space group, Zhou *et al.*<sup>100</sup> reported the structure and optical properties of  $\text{Cs}_2\text{SnCl}_{6-x}\text{Br}_x$  perovskite with an  $Fm\bar{3}m$  space group for photodetector application. Millimeter-sized  $\text{Cs}_2\text{SnCl}_{6-x}\text{Br}_x$  single crystals were grown by the hydrothermal method (see Fig. 4d). The transparent colour continuously changes from transparent to yellow and finally dark red by changing the halide ratio from Cl to Br. Narrowband single-crystal photodetectors using  $\text{Cs}_2\text{SnCl}_{6-x}\text{Br}_x$  crystals showed a high detectivity of  $\approx 2.71 \times 10^{10}$  Jones, with narrowband photodetection (full-width at half-maximum  $\approx 45$  nm) and high ion diffusion barriers. Moreover, the response spectra are continuously tuned from near violet to orange depending on the variation of the bandgap of the single crystals by changing the halide compositions. The strong surface charge recombination of the excess carriers near the crystal surfaces produced by short-wavelength light elucidates the narrowband photodetection behaviour. However, the instability of tin-based perovskites, further developing their single crystal form, remains the main challenge as well.

This section provided a new paradigm in designing new nano- and single crystals tin-based stable and high-performance perovskite derivatives for optoelectronics applications.

## 2.5. Chemical stability and degradation mechanism

Besides enormous developments in tin-based perovskites, their poor stability in  $\text{O}_2$  and  $\text{H}_2\text{O}$  environments remains a critical obstacle towards practical application (Fig. 5a). Therefore, similar to Pb-based perovskites,<sup>101–103</sup> fully understanding the degradation mechanism is reasonably necessary to solve the stability issue in this type of perovskites. Generally, as discussed, the facile oxidation of  $\text{Sn}^{2+}$  to  $\text{Sn}^{4+}$  was identified as the main instability reason of these materials, which leads to deteriorating the thin film morphology and optoelectronic properties, as well as high-density p-type doping.<sup>104–106</sup> Therefore, considering all the factors that can minimize  $\text{Sn}^{4+}$  formation is very important to improve the stability of tin-based perovskites.

In contrast to lead-based perovskites, the degradation mechanism of tin-based perovskites is not well described so far and requires a more detailed understanding.<sup>107</sup> Different reports predicted different by-products for  $\text{ASnI}_3$  ( $\text{A} = \text{Cs}^+$ ,  $\text{MA}^+$  or  $\text{FA}^+$ ) perovskites degradation. For example, some reports emphasized that  $\text{A}_2\text{SnI}_6$  and  $\text{SnO}_2$  are the main degradation byproducts,<sup>32,108–110</sup> while others suggested  $\text{SnI}_4$ ,  $\text{SnO}_2$ , and  $\text{Al}$ .<sup>111,112</sup> However, recently, Islam *et al.* reported that  $\text{SnI}_4$ -richer tin-based perovskite thin films undergo faster degradation under ambient conditions, suggesting the  $\text{SnI}_4$  as the significant contributor to this degradation due to its higher reactivity with water and oxygen than other by-products, *i.e.*,  $\text{A}_2\text{SnI}_6$ ,  $\text{SnO}_2$ , and  $\text{FAI}$ .<sup>113</sup> Therefore, they established a cyclic degradation mechanism for  $\text{ASnI}_3$ , emphasizing the dominant role of the  $\text{SnI}_4$  by-product. As shown in Fig. 5b, the  $\text{SnI}_4$  in thin film readily converts to  $\text{I}_2$  *via* a two-step process, first producing  $\text{HI}$  by its hydrolysis reaction in the presence of water and second producing  $\text{I}_2$  by  $\text{HI}$  oxidation in the presence of oxygen.

So far, strategies have been explored to address these issues and suppress  $\text{Sn}^{4+}$  formation, *i.e.*, prohibit  $\text{Sn}^{2+}$  oxidation in tin-based perovskites.<sup>24,31,114</sup> Various  $\text{SnX}_2$  ( $\text{X} = \text{F}, \text{Cl}, \text{Br}, \text{I}, \text{SCN}$ ) additives have been introduced in tin-based perovskites to suppress their oxidation. Firstly,  $\text{SnF}_2$  has shown a great potential to be a suitable additive for minimizing the  $\text{Sn}^{4+}$  amount and Sn vacancies in tin-based thin films.<sup>115,116</sup> Moreover,  $\text{SnCl}_2$  and  $\text{SnI}_2$  also have been used as  $\text{Sn}^{2+}$  compensators to decrease tin vacancies in perovskite thin films and enhance the photovoltaic performance of tin-based PSCs.<sup>117–120</sup> Besides the positive effect of  $\text{SnX}_2$  additives in tin-based perovskites, still their performing mechanisms need to be investigated in-depth in the future.

Unfortunately, even during the precursor preparation, due to the impurity of precursor components, some  $\text{Sn}^{4+}$  ions could form, which need to be converted back to  $\text{Sn}^{2+}$  again.<sup>121</sup> It has been demonstrated that adding a small amount of metallic tin powder to the perovskite precursor can effectively convert  $\text{Sn}^{4+}$  to  $\text{Sn}^{2+}$  ions *via* a comproportionation reaction, *i.e.*,  $\text{Sn} + \text{Sn}^{4+} \rightarrow$



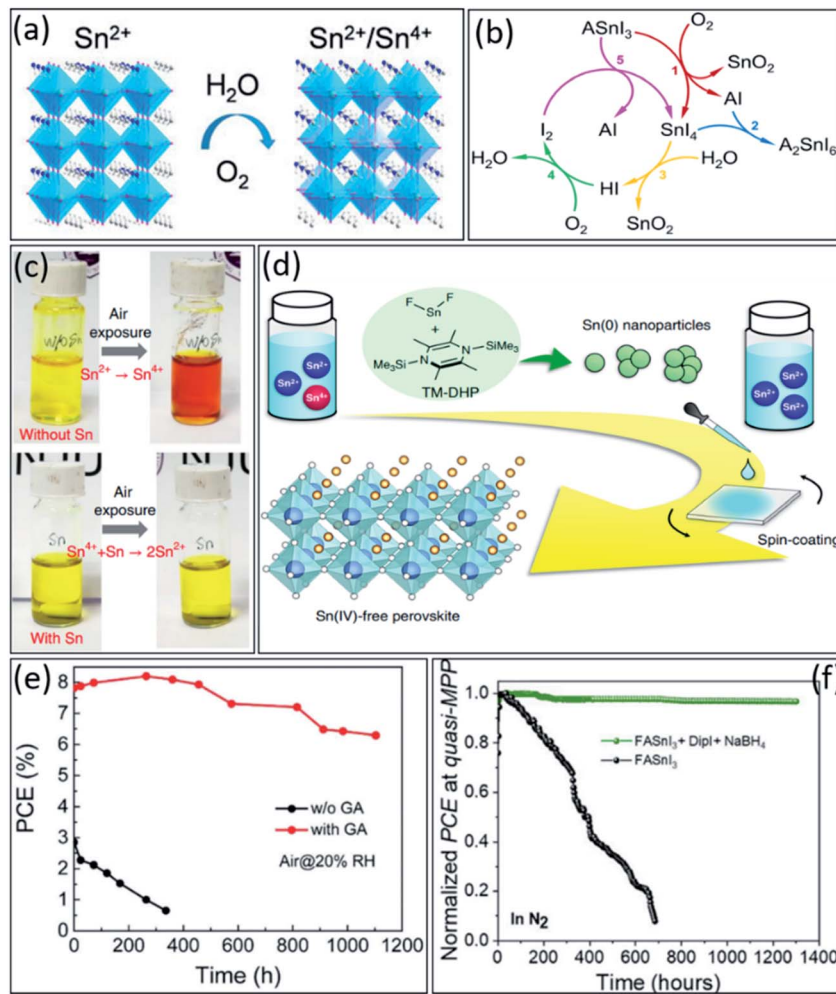


Fig. 5 (a) The schematic illustration of tin-based perovskite oxidation in the presence of water and oxygen.<sup>70</sup> Copyright 2021, APL materials. (b) The schematic illustration of the proposed cyclic tin-based perovskite degradation mechanism under ambient air exposure.<sup>113</sup> Copyright 2021, Springer Nature. (c) The photographs of tin-based perovskite precursors without and with tin powder as additive.<sup>45</sup> Copyright 2019, Springer Nature. (d) The schematic illustration of the mechanism of removing the residual Sn<sup>4+</sup> impurities from tin-based perovskites.<sup>46</sup> Copyright 2020, Springer Nature. (e) Long-term stability evolution of unencapsulated tin-based PSCs (stored in the air, RH ~20%).<sup>122</sup> Copyright 2020, American Chemical Society. (f) Stability comparison at MPP in N<sub>2</sub> atmosphere of the unencapsulated FASnI<sub>3</sub> and FASnI<sub>3</sub> + DipI + NaBH<sub>4</sub> devices under continuous illumination.<sup>124</sup> Copyright 2022, Elsevier.

2Sn<sup>2+</sup> (see Fig. 5c, the red colour of perovskite solution converted to yellow after the reaction).<sup>45</sup> Moreover, that Sn<sup>4+</sup> impurities could convert to Sn<sup>0</sup> nanoparticles (NPs) by adding 1,4-bis(trimethylsilyl)-2,3,5,6-tetramethyl-1,4-dihydropyrazine (TM-DHP) to the perovskite precursor, achieving an Sn<sup>4+</sup> free tin-based perovskite thin film (Fig. 5d).<sup>46</sup>

Organic antioxidant materials also can be used to suppress Sn<sup>2+</sup> oxidation. For example, gallic acid (GA) has been added to perovskite precursors as an efficient antioxidant to achieve highly stable tin-based PSCs.<sup>122</sup> The hydroxyl groups (−OH) on the aromatic ring in the GA chemical structure scavenge the oxygen molecules by donating hydrogen atoms. Due to this antioxidant effect, unencapsulated FASnI<sub>3</sub>-GA-based solar cells showed over 80% stability after storing in the air for 1000 h, which is the best air stability of tin-based PSCs so far (Fig. 5e). Very recently, Sanchez-Diaz *et al.* introduced a new chemical engineering approach to prevent the premature degradation of

tin-based perovskites.<sup>123</sup> They demonstrated that adding dipropylammonium iodide (DipI) together with sodium borohydride (NaBH<sub>4</sub>) as a well-known reducing agent to FASnI<sub>3</sub> precursor could suppress the oxidation of Sn<sup>2+</sup> into Sn<sup>4+</sup> during the solution processing, which promotes an improved film crystallization and minimizes the number of crystalline defects. As a result, 1300 h stability at MPP (under N<sub>2</sub> atmosphere) with retaining 96% of the initial PCE was achieved (see Fig. 5d).

However, besides many efforts to suppress the oxidation of tin-based thin films, this problem still is not entirely solved and needs to be investigated.

### 3. Tin-based perovskite devices

#### 3.1. Solar cells

Lead toxicity could be the main obstacle to perovskite commercialization. If alternative elements are sought, this is



very critical to consider both how to keep the device performance and stability simultaneously.<sup>23,106,109,125</sup> As mentioned, numerous environmentally friendly elements such as  $\text{Sn}^{2+}$ ,  $\text{Ge}^{2+}$ ,  $\text{Cu}^{2+}$ ,  $\text{Bi}^{3+}$ , and  $\text{Sb}^{3+}$  have been explored.<sup>126–128</sup> Among them, tin-based perovskites being the most promising.<sup>36,129</sup> However, despite their excellent photophysical properties, the best-achieved PCEs for tin-based PSCs with 3D perovskite structures are less than 10%, which is still very far from the lead-based counterpart.<sup>130,131</sup> Although the best PCE of 14.8% has been achieved for 2D/3D tin-based PSCs due to better stability than 3D structure,<sup>132</sup> however, the used spacer cations in structure decrease the charge transport and could confine further PCE improvement.

So far, many tin-based perovskite structures and compositions have been explored for solar cell application. In 2014, M. H. Kumar *et al.*<sup>125</sup> fabricated the  $\text{CsSnI}_3$  tin-based PSCs, with a bandgap of 1.3 eV, by adapted dye-sensitized solar cells device structure, achieving 2.0% efficiency (Fig. 6a). Afterwards, Koh *et al.*<sup>116</sup> achieved a PCE of 2.1% with the same device structure by changing the perovskite composition to  $\text{FASnI}_3$  with a bandgap of 1.41 eV (see Fig. 6b). Up to this point, tin-based perovskite was still used in regular device structure, *i.e.*, n-i-p.

However, it was realized that the most common hole transporter materials such as 2,2',7,7-tetrakis(*N,N*-di-p-methoxyphenylamino)-9,9-spirobifluorene (Spiro-OMeTAD) and poly(triarylamine) (PTAA) in n-i-p structure, typically contain lithium (Li) and/or cobalt (Co) salts additives, which could damage the tin-based perovskite films and lead to poor device performance consequently.<sup>69,133,134</sup> Hence, Liao *et al.* reported  $\text{FASnI}_3$  PSCs with an inverted solar cells structure, achieving efficiency up to 6.2% (see Fig. 6c).<sup>135</sup> Afterward, Zhao *et al.*<sup>136</sup> elevated the PCE of inverted tin-based PSCs to 8.1% by adding a small portion of  $\text{MA}^+$  into  $\text{FASnI}_3$  perovskite composition, *i.e.*,  $(\text{FA})_{0.75}(\text{MA})_{0.25}\text{SnI}_3$ . Moreover, Liu *et al.*<sup>54</sup> further improved the efficiency of this kind of PSCs beyond 9.0% by solvent engineering of perovskite film fabrication. In addition, Ran *et al.*<sup>137</sup> intercalate conjugated organic molecules in  $\text{FASnI}_3$  composition, reaching to PCE of 9.6% due to enlarged grain sizes, reduced trap density, preferential grain orientation, efficient charge extraction, and enhanced perovskite structural stability. Unlike the former reports, Jiang *et al.*<sup>79</sup> explored the influence of different electron transport layers on mixed 2D/3D tin-based PSCs performance, reaching a PCE of 12.4% with ultra-high open-circuit voltage at 0.94 V. During the development of tin-based PSCs, similar to Pb-based PSCs,<sup>138,139</sup> the research direction has shifted from the device structure to the interface, as well as, the charge transport layers. Still, the biggest problem remains in maintaining stability and fabricating a perfect film. Given this, the method and composition of the tin-based perovskites have been reconsidered. Considering the fact of easy oxidation of tin from Sn(II) to Sn(IV) and creating bulk defects in perovskite thin film, Yu *et al.*<sup>75</sup> provided a general and effective strategy to modulate the microstructure of 2D/3D heterogeneous tin-based perovskite by partially replacing formamidine iodide (FAI) with fluorinated phenethylammonium bromide (FPEABr) in  $\text{FASnI}_3$  perovskite, reaching a certified PCE over 14.0% (see Fig. 6d). Focusing on the

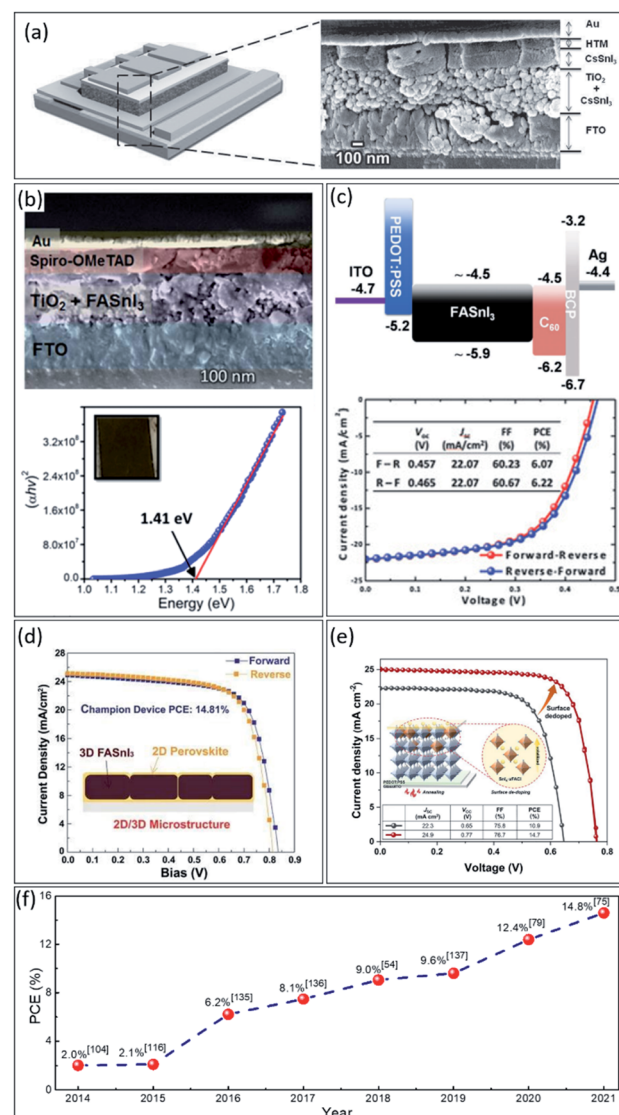


Fig. 6 (a) Schematic and cross-section FESEM image of the tin-based device structure.<sup>125</sup> Copyright 2014, Wiley. (b) Cross-sectional FE-SEM image of the full device with FTO/TiO<sub>2</sub>/FASnI<sub>3</sub>/spiro-OMe-TAD/Au structure and the Tauc plot of the FASnI<sub>3</sub> film showing its absorption onset.<sup>116</sup> Copyright 2015, The Royal Society of Chemistry. (c) Schematic of the energy level diagram of FASnI<sub>3</sub> PSC and the corresponding  $J-V$  characteristic.<sup>135</sup> Copyright 2016, Wiley. (d) The forward and reverse  $J-V$  scans of the champion of the tin-based PSC with 2D/3D structure.<sup>75</sup> Copyright 2021, Wiley. (e) The  $J-V$  characteristics of tin-based PSCs with and without surface doping.<sup>141</sup> Copyright 2022, Wiley. (f) Power conversion efficiency record tracking of tin-perovskite solar cells.

problems of limited carrier diffusion length and poor film morphology of tin-based perovskite films, Jiang *et al.*<sup>140</sup> designed a synthetic route for an *in situ* reaction of the metal Sn and I<sub>2</sub> in DMSO solvent, which produced a highly coordinated  $\text{SnI}_2\text{-}(\text{DMSO})_x$  adduct in a well-dispersed perovskite precursor solution. This adduct guides the out-of-plane crystal orientation and promotes the homogeneous growth of polycrystalline perovskite films, increasing the electron diffusion length from



$210 \pm 20$  nm to  $290 \pm 20$  nm and achieving a certified efficiency of 14.6%. Moreover, very recently, Zhou *et al.*<sup>141</sup> reported a new engineering concept, called chemo-thermal surface de-doping, to suppress the deleterious Sn(IV) self-doping, addressing the major obstacle of tin-based PSCs, leading to champion efficiency of 14.8% (see Fig. 6e). Finally, the efficiency records development of tin-based PSCs for each year is presented in Fig. 6f.

### 3.2. Light-emitting devices

Display technology has been developed for a long time; however, self-luminous displays have attracted attention in recent years, entirely attributable to the development and progress of light-emitting diode (LED) technology.<sup>142,143</sup> Due to the new demands of modern society for screen-adapted portable devices and wearable devices, the commercialization of organic light-emitting diodes (OLEDs) has been highly explored. However, the wide linewidths ( $>50$  nm) of organic emitters limit the attainable colour gamut.<sup>144</sup> This requires exploring other alternative materials for OLEDs application. The halide perovskite materials with excellent optoelectronic properties and ease of solution process thin films could fulfil the essential requirements to be introduced as an appropriate alternative for LED applications.<sup>38</sup>

The lead-based perovskite light-emitting diodes (PeLEDs) have been highly explored; however, the toxicity problem of lead could confine their further development.<sup>145</sup> Therefore, adopting the non-toxic tin-based perovskites from PSCs research to PeLEDs is reasonably necessary. The brightness, chromaticity, and lumens could be the technical advantages for developing PeLEDs. Due to the limited low bandgap, the tin-based PeLEDs have been studied mainly in the red-light regions.

In 2020, Liang *et al.*<sup>112</sup> used tin-based 2D perovskites to fabricate ultrapure and stable red emission devices, creating a new milestone in exploring PeLED progress. They identified the main oxidation pathway of  $\text{Sn}^{2+}$  in perovskite film could be suppressed by moderating the reduction properties and forming the stable complexes in perovskite precursors, which increases the energy barrier of oxidation. Specifically, the tin oxidation was inhibited with the help of  $\text{H}_3\text{PO}_2$ , which also improved the film quality by promoting crystal growth during the film formation process (see Fig. 7a). As a result, the optimized PeLEDs reached a maximum luminance of  $70 \text{ cd m}^{-2}$  under  $5.8 \text{ V}$ , giving an EQE of 0.3%, the highest reported brightness, and efficiency among red lead-free PeLEDs (see the EQE versus current density graph in Fig. 7a). Nevertheless, as shown in Fig. 7a, the Commission Internationale de l'Eclairage (CIE)  $x, y$  coordinates of the best-fabricated PeLEDs were (0.706, 0.294), which are closely matched to the Rec. 2020 red standard of (0.708, 0.292).<sup>146</sup> In another work, Lu *et al.*<sup>147</sup> reported the flexible near-infrared tin-based  $\text{CsSnI}_3$  PeLED. A dendritic  $\text{CsSnI}_3$  perovskite structure was sandwiched between PEDOT:PSS and B3PyMPM as the hole and electron transport layers. As schematically illustrated in Fig. 7b, the bulk  $\text{CsSnI}_3$  with flat morphology reduces excitons due to the nondirective diffusion of excess holes. Therefore, they suggested reducing

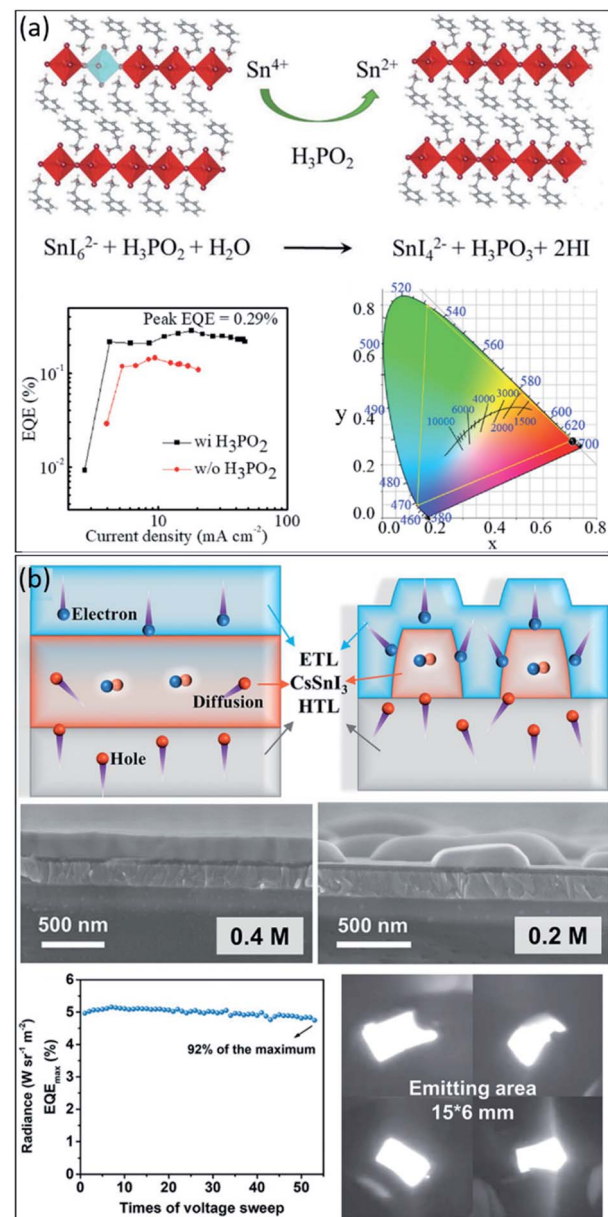


Fig. 7 (a) The proposed mechanism of  $\text{Sn}^{4+}$  reduction to  $\text{Sn}^{2+}$  using  $\text{H}_3\text{PO}_2$  additive, the EQE versus current density of PeLEDs with and without  $\text{H}_3\text{PO}_2$ , and the corresponding CIE coordinate of the device.<sup>112</sup> Copyright 2020, Wiley. (b) Schematic illustration of the charge carriers transport and recombination in the compact and dendritic  $\text{CsSnI}_3$  Pero-LEDs, cross-sectional SEM images of the structured films with 0.4 M and 0.2 M  $\text{CsSnI}_3$  concentrations, the  $\text{EQE}_{\text{max}}$  curve, and photographs of the lighting flexible 0.2 M  $\text{CsSnI}_3$  Pero-LEDs.<sup>148</sup> Copyright 2021, Wiley.

the  $\text{CsSnI}_3$  crystal size to confine the holes in the device, leading to the increased injection of electrons. For this purpose, they prepared dendritic  $\text{CsSnI}_3$  film by readily controlling the concentrations of the precursor up to 0.2 M (see SEM images in Fig. 7b). By utilizing this dendritic structure, a highly efficient lead-free NIR PeLED with a record external quantum efficiency (EQE) of 5.4% was achieved (Fig. 7b). Most importantly, the dendritic structure shows excellent advantages in flexible



devices, with almost no morphological change after 2000 bending cycles. The fabricated PeLED can maintain 93.4% of the initial EQE after 50 bends. Fig. 7b shows a photograph of fabricated PeLED with an emitting area of  $15 \times 6$  mm. In summary, we believe lead-free perovskite light-emitting devices show promise in the future.

### 3.3. Detectors and scintillators

One can use a detector that detects the photocurrent created by X-ray excitation to detect X-rays. In scintillators, however, the incoming X-ray or gamma-ray radiation can excite the electrons to the higher energy electronic levels by which emission occurs after thermalization and cooling down of the electrons.<sup>18</sup> The outgoing emission can be detected by a photomultiplier tube. Stability, response time, sensitivity, cost, safety and toxicity, ease of growth, processability, transparency, high light output, high radiation stopping power are among the factors which are considered for evaluation of a promising scintillator; among them, many are in common for the X-ray detectors.<sup>18</sup>

Recently, halide perovskite-based detectors and scintillators have been considered low-cost and promising materials for medical imaging applications.<sup>149</sup> In a direct conversion of X-rays into electrical signals, *i.e.*, in conventional detectors such as silicon,  $\text{PbI}_2$ ,  $\text{HgI}_2$ ,  $\text{CdTe}$ , and  $\text{CdZnTe}$ , there are limitations either in stopping power, stability, or having a significant signal to noise ratio. In scintillators, indirect conversion of X-ray or gamma-ray photons into the electrical signals occurs in which the excited electrons re-emit photons which are detected by a photomultiplier tube. The implemented conventional devices are successfully developed; however, they still show drawbacks such as high-cost and complicated fabrication methods and non-tunable scintillation properties.<sup>150</sup>

In comparison, halide perovskites can be fabricated by low-cost methods with tunable properties. Recently, lead halide perovskite materials have been used as very attractive and efficient alternatives for X-ray detector and scintillator devices making similar or even better detection qualities while having advantages of tunable bandgap, spectacular physical properties, excellent X-ray absorption capacity, very convenient sensitivity, and ultra-low detection limits.<sup>151</sup> The perovskite scintillators

also have near-unity photoluminescence quantum yield (PLYQ), high radiation, high light yield, fast scintillation response, rather high stability.<sup>18</sup>

As lead-based halide perovskites are still the most investigated and efficient materials yet, tin-based perovskites have been considered the main replica for the toxic lead with their own drawbacks and benefits compared to the lead counterpart.<sup>18</sup> For example, tin halides possess worse X-ray absorption capability since the absorption stopping power for X-rays is a quadratic power function of atomic number; however, it is very feasible making thicker samples. As the samples became thicker, the diffusion length of carriers needs to be improved that is a function of  $\tau \cdot \mu$  product wherein  $\tau$  and  $\mu$  are mobility and the lifetime of the carriers, respectively. The mobility  $\tau$  is higher in the case of tin-based halide perovskites than the lead perovskites. However, the lifetime is more material composition dependent on a parameter that needs further study.

Moreover, the bandgap is not a very important parameter for scintillation. Both lead and tin perovskites have the same flexibility for bandgap tuning through compositional engineering for special photomultiplier tube sensitivities. Still, some of the conventional scintillators such as  $\text{CsI:Ti}$  and  $\text{YAlO}_3:\text{Ce}$  show emissions that are not appropriate for many detectors used in scintillation setups; however, the bandgap tunability of halide perovskites will contribute to making faster and more powerful responses by tuning the bandgap value close the most sensitive point of the detector.

The transport time and bulk resistivity became important for X-ray detectors to have a faster response and lower noise ratio. The bulk resistivity, proportional to the inverse of the conductivity, is lower for the  $\text{MAPbI}_3$  than  $\text{MASnI}_3$  (Table 1).

A photon yield of up to 296 000 photon per MeV at lower temperatures for  $\text{MAPbI}_3$  has been recorded.<sup>152</sup>  $\text{MAPbBr}_3$  is the most investigated perovskite material for the scintillators possessing a very fast response—as fast as 1 ns at low temperatures—a high yield of more than 90 000 photon per MeV.<sup>17</sup> The emitted wavelength is close to the highest sensitivities for the PMTs, but the  $\text{MAPbCl}_3$  bandgap is even more suitable. There is much ongoing research in material engineering to obtain perovskite scintillators with superior physical properties and better performance.

Table 1 Physical properties of methylammonium tin perovskite and comparison the lead-based counterpart

Properties	$\text{MAPbI}_3$ (ref. 27)	$\text{MASnI}_3$ (ref. 153)
Optical band gap	1.6 eV	1.2 eV
Crystal structure (room temperature)	$I4/mcm$ (tetragonal)	Tetragonal
Electron mobility	$0.06\text{--}1.4 \text{ cm}^2 \text{ V}^{-1} \text{ s}^{-1}$	$1.6 \text{ cm}^2 \text{ V}^{-1} \text{ s}^{-1}$
Hole mobility	$0.6\text{--}1.4 \text{ cm}^2 \text{ V}^{-1} \text{ s}^{-1}$	$1.6 \text{ cm}^2 \text{ V}^{-1} \text{ s}^{-1}$
Diffusion length	1 micrometre	500 nm
Typical lifetime	5 ns	5–9 ns
Absorption coefficient	$3 \times 10^5 \text{ cm}^{-1}$	$1.82 \times 10^4 \text{ cm}^{-1}$
Exciton binding energy	2–20 meV	29 meV
Carrier cooling time scale	1 ps	—
Typical range of bandgaps for cation/exchange	1.4 to 1.75 eV	1.2–1.4 eV
Carrier concentration	$10^9 \text{ cm}^3$	$10^{14} \text{ cm}^3$
Electric conductivity	$3 \times 10^{-4} \text{ S m}^{-1}$	$5 \times 10^{-2} \text{ S m}^{-1}$



## 4. Conclusions

Halide perovskites have emerged as an exceptional material with excellent optoelectronic properties such as high optical absorption coefficients, tunable bandgaps, low exciton binding energies, and long-range carrier diffusion. As a result, the solution-processed optoelectronic devices with these materials, such as perovskite solar cells (PSCs) and light-emitting diodes (LEDs), have shown excellent performances. Despite the extensive effort and significant progress, the toxicity of lead elements in perovskite composition remains the main obstacle to the widespread applications of perovskite materials. Among various alternative metal ions to replace lead for environmentally benign perovskites, tin element from the same group in the periodical table has been considered the most promising alternative to fabricate lead-free perovskites with similar optoelectronic properties qualities to lead-based counterparts; however, with much lower toxicity issues. So far, tin-based perovskites have been successfully used not only for solar cells but also for other optoelectronic applications. This perspective covered the critical developments of tin-based perovskite, as well as, drawbacks and challenges based on their physical properties. Firstly, we provided a comprehensive understanding of the fundamental atomic properties of tin-based perovskite and compared it to the lead-based counterpart. Based on this, we explored the possible degradation mechanisms for tin-based perovskites and suggested possible approaches for improving the stability of these materials.

The quality of the tin-based film is highly related to controlling the nucleation and growth processes. Solvent and additive engineering of tin-based perovskite precursors are critical to suppressing  $\text{Sn}^{2+}$  oxidation as the main challenge of tin-based PSCs. Moreover, perovskite phase engineering from 3D to 2D or a combination of 2D/3D is an efficient approach to suppress tin oxidation, improve efficiency, and improve stability. The efficiency progress of tin-based PSCs from the beginning until the present is explored, providing the efficiency records for each year. So far, by introducing reducing agents and undertaking compositional engineering, the device stability reached over 1300 h. However, still, device stability remains the main issue for the technology commercialization of tin-based PSCs.

Besides the thin films, we investigated the research progress of nanocrystals and single crystals tin-based perovskites, considering the challenges of synthesis and stabilization of these materials. Additionally, we investigated beyond the photovoltaic application of tin-based perovskites as light-emitting devices, detectors, and scintillators. Regarding the light-emitting devices, we showed that the tin-based perovskites could fulfil the essential requirements for this application as well. We showed that a new milestone in tin-based perovskite LEDs progress could be achieved by changing the 3D to 2D feature, delivering ultrapure and stable red emission devices. We also showed that tin-based perovskites could be used for detectors and scintillators applications as low-cost and promising materials for medical imaging applications.

## Author contributions

M. M. B. was the main responsible for writing the perspective. W. Z., R. I. and M. P. were involved in writing a few parts of the perspective. All co-authors discussed the paper and revised the manuscript. M. S. was involved in providing the main idea and supervising the work.

## Conflicts of interest

The authors declare no conflict of interest.

## Acknowledgements

M. S. thanks the German Research Foundation (DFG) for funding (SPP2196, 431314977/GRK 2642). M. S. acknowledges funding by ProperPhotoMile. Project ProperPhotoMile is supported under the umbrella of SOLAR-ERA.NET Cofund 2 by The Spanish Ministry of Science and Education and the AEI under the project PCI2020-112185 and CDTI project number IDI-20210171; the Federal Ministry for Economic Affairs and Energy on the basis of a decision by the German Bundestag project number FKZ 03EE1070B and FKZ 03EE1070A and the Israel Ministry of Energy with project number 220-11-031. SOLAR-ERA.NET is supported by the European Commission within the EU Framework Programme for Research and Innovation HORIZON 2020 (Cofund ERA-NET Action, No. 786483).

## References

- 1 A. K. Jena, A. Kulkarni and T. Miyasaka, *Chem. Rev.*, 2019, **119**, 3036–3103.
- 2 J. Y. Kim, J.-W. Lee, H. S. Jung, H. Shin and N.-G. Park, *Chem. Rev.*, 2020, **120**, 7867–7918.
- 3 W. Dieter, *Z. Naturforsch. B Chem. Sci.*, 1978, **33**, 1443–1445.
- 4 H. L. Wells, *Z. Anorg. Chem.*, 1893, **3**, 195–210.
- 5 K. Liang and D. B. Mitzi, Luminescent Organic-Inorganic Perovskites With A Divalent Rare Earth Metal Halide Framework, *US Pat.*, US5882548A, 1999, vol. 20, pp. 1–6.
- 6 C. R. Kagan, D. B. Mitzi and C. D. Dimitrakopoulos, *Science*, 1999, **286**, 945–947.
- 7 K. Liang, D. B. Mitzi and M. T. Prikas, *Chem. Mater.*, 1998, **10**, 403–411.
- 8 K. Yamada, H. Kawaguchi, T. Matsui, T. Okuda and S. Ichiba, *Bull. Chem. Soc. Jpn.*, 1990, **63**, 2521–2525.
- 9 K. Yamada, T. Hayashi, T. Umehara, T. Okuda and S. Ichiba, *Bull. Chem. Soc. Jpn.*, 1987, **60**, 4203.
- 10 J. Calabrese, N. L. Jones, R. L. Harlow, N. Herron, D. L. Thorn and Y. Wang, *J. Am. Chem. Soc.*, 1991, **113**, 2328–2330.
- 11 A. Kojima, K. Teshima, Y. Shirai and T. Miyasaka, *J. Am. Chem. Soc.*, 2009, **131**, 6050–6051.
- 12 M. M. Lee, J. Teuscher, T. Miyasaka, T. N. Murakami and H. J. Snaith, *Science*, 2012, **338**, 643–647.
- 13 *Nat. Mater.*, 2014, **13**, 837.
- 14 Best Research-Cell Efficiencies, National Renewable Energy Laboratory (NREL), Natl. Renew. Energy Lab., 2022, <https://>



[www.nrel.gov/pv/assets/pdfs/best-research-cell-efficiencies-rev220126.pdf](http://www.nrel.gov/pv/assets/pdfs/best-research-cell-efficiencies-rev220126.pdf), accessed 2022-04-18.

15 H. C. Hsu, Z. Y. Wu, Y. Y. Chen and L. J. Lin, *J. Phys. Chem. C*, 2021, **125**, 5180–5184.

16 Z.-K. Tan, R. S. Moghaddam, M. L. Lai, P. Docampo, R. Higler, F. Deschler, M. Price, A. Sadhanala, L. M. Pazos, D. Credgington, F. Hanusch, T. Bein, H. J. Snaith and R. H. Friend, *Nat. Nanotechnol.*, 2014, 1–6.

17 V. B. Mykhaylyk, H. Kraus and M. Saliba, *Mater. Horiz.*, 2019, **6**, 1740–1747.

18 Y. Zhou, J. Chen, O. M. Bakr and O. F. Mohammed, *ACS Energy Lett.*, 2021, **6**, 739–768.

19 H. Min, D. Y. Lee, J. Kim, G. Kim, K. S. Lee, J. Kim, M. J. Paik, Y. K. Kim, K. S. Kim, M. G. Kim, T. J. Shin and S. Il Seok, *Nature*, 2021, **598**, 444–450.

20 J. J. Yoo, G. Seo, M. R. Chua, T. G. Park, Y. Lu, F. Rotermund, Y.-K. Kim, C. S. Moon, N. J. Jeon, J.-P. Correa-Baena, V. Bulović, S. S. Shin, M. G. Bawendi and J. Seo, *Nature*, 2021, **590**, 587–593.

21 M. Jeong, I. W. Choi, E. M. Go, Y. Cho, M. Kim, B. Lee, S. Jeong, Y. Jo, H. W. Choi, J. Lee, J. Bae, S. K. Kwak, D. S. Kim and C. Yang, *Science*, 2020, **1620**, 1615–1620.

22 M. Grätzel, *Nat. Mater.*, 2014, **13**, 838–842.

23 A. Abate, *Joule*, 2017, **1**, 659–664.

24 S. A. U. Hasan, D. S. Lee, S. H. Im and K.-H. Hong, *Sol. RRL*, 2020, **4**, 1900310.

25 M. Pazoki, A. Röckert, M. J. Wolf, R. Imani, T. Edvinsson and J. Kullgren, *J. Mater. Chem. A*, 2017, 23131–23138.

26 M. Pazoki, T. J. Jacobsson, A. Hagfeldt, G. Boschloo and T. Edvinsson, *Phys. Rev. B*, 2016, **93**, 144105.

27 M. Pazoki and T. Edvinsson, *Sustain. Energy Fuels*, 2018, 1–16.

28 F. De Angelis, *ACS Energy Lett.*, 2021, **6**, 1586–1587.

29 T. J. Jacobsson, M. Pazoki, A. Hagfeldt and T. Edvinsson, *J. Phys. Chem. C*, 2015, **119**, 25673–25683.

30 R. Nie, R. R. Sumukam, S. H. Reddy, M. Banavoth and S. Il Seok, *Energy Environ. Sci.*, 2020, **13**, 2363–2385.

31 Y. Yan, T. Pullerits, K. Zheng and Z. Liang, *ACS Energy Lett.*, 2020, **5**, 2052–2086.

32 C. C. Stoumpos, C. D. Malliakas and M. G. Kanatzidis, *Inorg. Chem.*, 2013, **52**, 9019–9038.

33 D. Sabba, H. K. Mulmudi, R. R. Prabhakar, T. Krishnamoorthy, T. Baikie, P. P. Boix, S. Mhaisalkar and N. Mathews, *J. Phys. Chem. C*, 2015, **119**, 1763–1767.

34 X. Jiang, Z. Zang, Y. Zhou, H. Li, Q. Wei and Z. Ning, *Acc. Mater. Res.*, 2021, **2**, 210–219.

35 J. Cao and F. Yan, *Energy Environ. Sci.*, 2021, **14**, 1286–1325.

36 Q. Tai, X. Guo, G. Tang, P. You, T.-W. Ng, D. Shen, J. Cao, C.-K. Liu, N. Wang, Y. Zhu, C.-S. Lee and F. Yan, *Angew. Chem., Int. Ed.*, 2019, **58**, 806–810.

37 L. E. Mundt, J. Tong, A. F. Palmstrom, S. P. Dunfield, K. Zhu, J. J. Berry, L. T. Schelhas and E. L. Ratcliff, *ACS Energy Lett.*, 2020, **5**, 3344–3351.

38 M. I. Saidaminov, I. Spanopoulos, J. Abed, W. Ke, J. Wicks, M. G. Kanatzidis and E. H. Sargent, *ACS Energy Lett.*, 2020, **5**, 1153–1155.

39 M. Konstantakou and T. Stergiopoulos, *J. Mater. Chem. A*, 2017, **5**, 11518–11549.

40 P. Mahajan, R. Datt, W. Chung Tsoi, V. Gupta, A. Tomar and S. Arya, *Coord. Chem. Rev.*, 2021, **429**, 213633.

41 R. S. Drago, *J. Phys. Chem.*, 1958, **62**, 353–357.

42 A. Goyal, S. McKechnie, D. Pashov, W. Tumas, M. van Schilfgaarde and V. Stevanović, *Chem. Mater.*, 2018, **30**, 3920–3928.

43 Z. Xiao, Z. Song and Y. Yan, *Adv. Mater.*, 2019, **31**, 1803792.

44 M. Awais, R. L. Kirsch, V. Yeddu and M. I. Saidaminov, *ACS Mater. Lett.*, 2021, **3**, 299–307.

45 R. Lin, K. Xiao, Z. Qin, Q. Han, C. Zhang, M. Wei, M. I. Saidaminov, Y. Gao, J. Xu, M. Xiao, A. Li, J. Zhu, E. H. Sargent and H. Tan, *Nat. Energy*, 2019, **4**, 864–873.

46 T. Nakamura, S. Yakamaru, M. A. Truong, K. Kim, J. Liu, S. Hu, K. Otsuka, R. Hashimoto, R. Murdey, T. Sasamori, H. Do Kim, H. Ohkita, T. Handa, Y. Kanemitsu and A. Wakamiya, *Nat. Commun.*, 2020, **11**, 3008.

47 M. Awais, R. L. Kirsch, V. Yeddu and M. I. Saidaminov, *ACS Mater. Lett.*, 2021, **3**, 299–307.

48 Z. Saki, M. M. Byranvand, N. Taghavinia, M. Kedia and M. Saliba, *Energy Environ. Sci.*, 2021, **14**, 5690–5722.

49 F. Hao, C. C. Stoumpos, D. H. Cao, R. P. H. Chang and M. G. Kanatzidis, *Nat. Photonics*, 2014, **8**, 489–494.

50 N. J. Jeon, J. H. Noh, Y. C. Kim, W. S. Yang, S. Ryu and S. Il Seok, *Nat. Mater.*, 2014, **13**, 897–903.

51 F. Hao, C. C. Stoumpos, P. Guo, N. Zhou, T. J. Marks, R. P. H. Chang and M. G. Kanatzidis, *J. Am. Chem. Soc.*, 2015, **137**, 11445–11452.

52 M. M. Byranvand, S. Song, L. Pyeon, G. Kang, G. Y. Lee and T. Park, *Nano Energy*, 2017, **34**, 181–187.

53 N. Ahn, D. Y. Son, I. H. Jang, S. M. Kang, M. Choi and N. G. Park, *J. Am. Chem. Soc.*, 2015, **137**, 8696–8699.

54 X. Liu, K. Yan, D. Tan, X. Liang, H. Zhang and W. Huang, *ACS Energy Lett.*, 2018, **3**, 2701–2707.

55 H. Taherianfar, G. W. Kim, M. M. Byranvand, K. Choi, G. Kang, H. Choi, F. Tajabadi, N. Taghavinia and T. Park, *ACS Appl. Energy Mater.*, 2020, **3**, 1506–1514.

56 J. Liu, M. Ozaki, S. Yakamaru, T. Handa, R. Nishikubo, Y. Kanemitsu, A. Saeki, Y. Murata, R. Murdey and A. Wakamiya, *Angew. Chem., Int. Ed.*, 2018, **57**, 13221–13225.

57 M. M. Byranvand and M. Saliba, *Sol. RRL*, 2021, **5**, 2100295.

58 L. P. Junzhi Ye, M. Malekshahi Byranvand, C. Otero Martínez, R. L. Z. Hoye and M. Saliba, *Angew. Chem.*, 2021, **133**, 21804–21828.

59 S. J. Lee, S. S. Shin, Y. C. Kim, D. Kim, T. K. Ahn, J. H. Noh, J. Seo and S. Il Seok, *J. Am. Chem. Soc.*, 2016, **138**, 3974–3977.

60 L. Deng, K. Wang, H. Yang, H. Yu and B. Hu, *J. Phys. D: Appl. Phys.*, 2018, **51**, 475102.

61 P. Jun, W. Daniel, R. Yuhao, T. Mike, W. Yiliang, D. The, L. Qiaoling, L. Juntao, L. Teng, M. M. Arafat, L. O. L. Cheong, Z. Shenyou, L. Wenzhu, L. Yun, S. Heping, L. Li, K. Felipe, H. T. Nguyen, C. Duk-Yong, K. J. Weber, K. R. Catchpole and T. P. White, *Science*, 2021, **371**, 390–395.



62 C. Zhu, X. Niu, Y. Fu, N. Li, C. Hu, Y. Chen, X. He, G. Na, P. Liu, H. Zai, Y. Ge, Y. Lu, X. Ke, Y. Bai, S. Yang, P. Chen, Y. Li, M. Sui, L. Zhang, H. Zhou and Q. Chen, *Nat. Commun.*, 2019, **10**, 815.

63 K. Nishimura, D. Hirotani, M. A. Kamarudin, Q. Shen, T. Toyoda, S. Iikubo, T. Minemoto, K. Yoshino and S. Hayase, *ACS Appl. Mater. Interfaces*, 2019, **11**, 31105–31110.

64 F. Hao, C. C. Stoumpos, P. Guo, N. Zhou, T. J. Marks, R. P. H. Chang and M. G. Kanatzidis, *J. Am. Chem. Soc.*, 2015, **137**, 11445–11452.

65 J. Liu, M. Ozaki, S. Yakumaru, T. Handa, R. Nishikubo, Y. Kanemitsu, A. Saeki, Y. Murata, R. Murdey and A. Wakamiya, *Angew. Chem., Int. Ed.*, 2018, **57**, 13221–13225.

66 X. Meng, J. Lin, X. Liu, X. He, Y. Wang, T. Noda, T. Wu, X. Yang and L. Han, *Adv. Mater.*, 2019, **31**, 1–7.

67 G. Grancini and M. K. Nazeeruddin, *Nat. Rev. Mater.*, 2019, **4**, 4–22.

68 Z. Wang, Q. Lin, F. P. Chmiel, N. Sakai, L. M. Herz and H. J. Snaith, *Nat. Energy*, 2017, **2**, 1–16.

69 L. Ma, M. G. Ju, J. Dai and X. C. Zeng, *Nanoscale*, 2018, **10**, 11314–11319.

70 T. Zhang, Q. Sun, X. Zhang, Y. Shen and M. Wang, *APL Mater.*, 2021, **9**, 20906.

71 H. Li, X. Jiang, Q. Wei, Z. Zang, M. Ma, F. Wang, W. Zhou and Z. Ning, *Angew. Chem., Int. Ed.*, 2021, **60**, 16330–16336.

72 J. Li, P. Hu, Y. Chen, Y. Li, M. Wei and M. Wei, *ACS Sustain. Chem. Eng.*, 2020, **8**, 8624–8628.

73 D. B. Mitzi, C. a. Feild, W. T. a. Harrison and a. M. Guloy, *Nature*, 1994, **369**, 467–469.

74 M. Li, W.-W. Zuo, Y.-G. Yang, M. H. Aldamasy, Q. Wang, S. H. T. Cruz, S.-L. Feng, M. Saliba, Z.-K. Wang and A. Abate, *ACS Energy Lett.*, 2020, **5**, 1923–1929.

75 B.-B. Yu, Z. Chen, Y. Zhu, Y. Wang, B. Han, G. Chen, X. Zhang, Z. Du and Z. He, *Adv. Mater.*, 2021, **33**, 2102055.

76 A. G. Ricciardulli, S. Yang, J. H. Smet and M. Saliba, *Nat. Mater.*, 2021, **20**, 1325–1336.

77 F. Zhang, Q. Zhang, X. Liu, Y. Hu, Z. Lou, Y. Hou and F. Teng, *ACS Appl. Mater. Interfaces*, 2021, **13**, 24272–24284.

78 F. Wang, X. Jiang, H. Chen, Y. Shang, H. Liu, J. Wei, W. Zhou, H. He, W. Liu and Z. Ning, *Joule*, 2018, **2**, 2732–2743.

79 X. Jiang, F. Wang, Q. Wei, H. Li, Y. Shang, W. Zhou, C. Wang, P. Cheng, Q. Chen, L. Chen and Z. Ning, *Nat. Commun.*, 2020, **11**, 1245.

80 H. Xu, Y. Jiang, T. He, S. Li, H. Wang, Y. Chen, M. Yuan and J. Chen, *Adv. Funct. Mater.*, 2019, **29**, 1807696.

81 H. Xu, Y. Jiang, T. He, S. Li, H. Wang, Y. Chen, M. Yuan and J. Chen, *Adv. Funct. Mater.*, 2019, **29**, 1807696.

82 Q. A. Akkerman, V. D’Innocenzo, S. Accornero, A. Scarpellini, A. Petrozza, M. Prato and L. Manna, *J. Am. Chem. Soc.*, 2015, **137**, 10276–10281.

83 F. Zhang, H. Zhong, C. Chen, X. Wu, X. Hu, H. Huang, J. Han, B. Zou and Y. Dong, *ACS Nano*, 2015, **9**, 4533–4542.

84 L. Protesescu, S. Yakunin, M. I. Bodnarchuk, F. Krieg, R. Caputo, C. H. Hendon, R. X. Yang, A. Walsh and M. V. Kovalenko, *Nano Lett.*, 2015, **15**, 3692–3696.

85 Q. Fan, G. V. Biesold-McGee, J. Ma, Q. Xu, S. Pan, J. Peng and Z. Lin, *Angew. Chem., Int. Ed.*, 2020, **59**, 1030–1046.

86 J.-K. Chen, B.-B. Zhang, Q. Liu, N. Shirahata, O. F. Mohammed, O. M. Bakr and H.-T. Sun, *ACS Mater. Lett.*, 2021, 1541–1557.

87 A. Dey, J. Ye, A. De, E. Debroye, S. K. Ha, E. Bladt, A. S. Kshirsagar, Z. Wang, J. Yin, Y. Wang, L. N. Quan, F. Yan, M. Gao, X. Li, J. Shamsi, T. Debnath, M. Cao, M. A. Scheel, S. Kumar, J. A. Steele, M. Gerhard, L. Chouhan, K. Xu, X. Wu, Y. Li, Y. Zhang, A. Dutta, C. Han, I. Vincon, A. L. Rogach, A. Nag, A. Samanta, B. A. Korgel, C.-J. Shih, D. R. Gamelin, D. H. Son, H. Zeng, H. Zhong, H. Sun, H. V. Demir, I. G. Scheblykin, I. Mora-Seró, J. K. Stolarczyk, J. Z. Zhang, J. Feldmann, J. Hofkens, J. M. Luther, J. Pérez-Prieto, L. Li, L. Manna, M. I. Bodnarchuk, M. V. Kovalenko, M. B. J. Roeffaers, N. Pradhan, O. F. Mohammed, O. M. Bakr, P. Yang, P. Müller-Buschbaum, P. V. Kamat, Q. Bao, Q. Zhang, R. Krahne, R. E. Galian, S. D. Stranks, S. Bals, V. Biju, W. A. Tisdale, Y. Yan, R. L. Z. Hoye and L. Polavarapu, *ACS Nano*, 2021, **15**, 10775–10981.

88 J. Shamsi, A. S. Urban, M. Imran, L. De Trizio and L. Manna, *Chem. Rev.*, 2019, **119**, 3296–3348.

89 T. C. Jellicoe, J. M. Richter, H. F. J. Glass, M. Tabachnyk, R. Brady, S. E. Dutton, A. Rao, R. H. Friend, D. Credgington, N. C. Greenham and M. L. Böhm, *J. Am. Chem. Soc.*, 2016, **138**, 2941–2944.

90 Q. Chen, N. De Marco, Y. Michael, T. Song, C. Chen and H. Zhao, *Nano Today*, 2015, **10**, 355–396.

91 J. De Roo, M. Ibáñez, P. Geiregat, G. Nedelcu, W. Walravens, J. Maes, J. C. Martins, I. Van Driessche, M. V. Kovalenko and Z. Hens, *ACS Nano*, 2016, **10**, 2071–2081.

92 H. Tsai, W. Nie, J. C. Blancon, C. C. Stoumpos, R. Asadpour, B. Harutyunyan, A. J. Neukirch, R. Verduzco, J. J. Crochet, S. Tretiak, L. Pedesseau, J. Even, M. A. Alam, G. Gupta, J. Lou, P. M. Ajayan, M. J. Bedzyk, M. G. Kanatzidis and A. D. Mohite, *Nature*, 2016, **536**, 312–317.

93 M. C. Weidman, M. Seitz, S. D. Stranks and W. A. Tisdale, *ACS Nano*, 2016, **10**, 7830–7839.

94 M. C. Weidman, M. Seitz, S. D. Stranks and W. A. Tisdale, *ACS Nano*, 2016, **10**, 7830–7839.

95 Q. Fan, G. V. Biesold-McGee, J. Ma, Q. Xu, S. Pan, J. Peng and Z. Lin, *Angew. Chem., Int. Ed.*, 2020, **59**, 1030–1046.

96 B. Chen, P. N. Rudd, S. Yang, Y. Yuan and J. Huang, *Chem. Soc. Rev.*, 2019, **48**, 3842–3867.

97 S. Trivedi, D. Prochowicz, N. Parikh, A. Mahapatra, M. K. Pandey, A. Kalam, M. M. Tavakoli and P. Yadav, *ACS Omega*, 2021, **6**, 1030–1042.

98 N. K. Tailor, S. Kar, P. Mishra, A. These, C. Kupfer, H. Hu, M. Awais, M. Saidaminov, M. I. Dar, C. Brabec and S. Satapathi, *ACS Mater. Lett.*, 2021, **3**, 1025–1080.

99 Y. Dang, Y. Zhou, X. Liu, D. Ju, S. Xia, H. Xia and X. Tao, *Angew. Chem., Int. Ed.*, 2016, **55**, 3447–3450.



100 J. Zhou, J. Luo, X. Rong, P. Wei, M. S. Molokeev, Y. Huang, J. Zhao, Q. Liu, X. Zhang, J. Tang and Z. Xia, *Adv. Opt. Mater.*, 2019, **7**, 1900139.

101 M. Mohammadi, S. Gholipour, M. Malekshahi Byranvand, Y. Abdi, N. Taghavinia and M. Saliba, *ACS Appl. Mater. Interfaces*, 2021, **13**, 45455–45464.

102 L. Schmidt-Mende, V. Dyakonov, S. Olthof, F. Ünlü, K. M. T. Lê, S. Mathur, A. D. Karabanov, D. C. Lupascu, L. M. Herz, A. Hinderhofer, F. Schreiber, A. Chernikov, D. A. Egger, O. Shargaieva, C. Cocchi, E. Unger, M. Saliba, M. M. Byranvand, M. Kroll, F. Nehm, K. Leo, A. Redinger, J. Höcker, T. Kirchartz, J. Warby, E. Gutierrez-Partida, D. Neher, M. Stolterfoht, U. Würfel, M. Unmüssig, J. Herterich, C. Baretzky, J. Mohanraj, M. Thelakkat, C. Maheu, W. Jaegermann, T. Mayer, J. Rieger, T. Fauster, D. Niesner, F. Yang, S. Albrecht, T. Riedl, A. Fakharuddin, M. Vasilopoulou, Y. Vaynzof, D. Moia, J. Maier, M. Franckevičius, V. Gulbinas, R. A. Kerner, L. Zhao, B. P. Rand, N. Glück, T. Bein, F. Matteocci, L. A. Castriotta, A. Di Carlo, M. Scheffler and C. Draxl, *APL Mater.*, 2021, **9**, 109202.

103 J. Lee, M. Malekshahi Byranvand, G. Kang, S. Y. Son, S. Song, G.-W. Kim and T. Park, *J. Am. Chem. Soc.*, 2017, **139**, 12175–12181.

104 M. H. Kumar, S. Dharani, W. L. Leong, P. P. Boix, R. Prabhakar, T. Baikie, C. Shi, H. Ding, R. Ramesh, M. Asta, M. Graetzel, S. G. Mhaisalkar and N. Mathews, *Adv. Mater.*, 2014, 7122–7127.

105 M. B. Johnston and L. M. Herz, *Acc. Chem. Res.*, 2016, **49**, 146–154.

106 W. Ke and M. G. Kanatzidis, *Nat. Commun.*, 2019, **10**, 965.

107 L. Lanzetta, N. Aristidou and S. A. Haque, *J. Phys. Chem. Lett.*, 2020, **11**, 574–585.

108 X. Qiu, B. Cao, S. Yuan, X. Chen, Z. Qiu, Y. Jiang, Q. Ye, H. Wang, H. Zeng, J. Liu and M. G. Kanatzidis, *Sol. Energy Mater. Sol. Cells*, 2017, **159**, 227–234.

109 W. Ke, C. C. Stoumpos and M. G. Kanatzidis, *Adv. Mater.*, 2019, **31**, 1803230.

110 D. J. Kubicki, D. Prochowicz, E. Salager, A. Rakhmatullin, C. P. Grey, L. Emsley and S. D. Stranks, *J. Am. Chem. Soc.*, 2020, **142**, 7813–7826.

111 T. Leijtens, R. Prasanna, A. Gold-Parker, M. F. Toney and M. D. McGehee, *ACS Energy Lett.*, 2017, **2**, 2159–2165.

112 H. Liang, F. Yuan, A. Johnston, C. Gao, H. Choubisa, Y. Gao, Y.-K. Wang, L. K. Sagar, B. Sun, P. Li, G. Bappi, B. Chen, J. Li, Y. Wang, Y. Dong, D. Ma, Y. Gao, Y. Liu, M. Yuan, M. I. Saidaminov, S. Hoogland, Z.-H. Lu and E. H. Sargent, *Adv. Sci.*, 2020, **7**, 1903213.

113 L. Lanzetta, T. Webb, N. Zibouche, X. Liang, D. Ding, G. Min, R. J. E. Westbrook, B. Gaggio, T. J. Macdonald, M. S. Islam and S. A. Haque, *Nat. Commun.*, 2021, **12**, 2853.

114 W.-F. Yang, F. Igbari, Y.-H. Lou, Z.-K. Wang and L.-S. Liao, *Adv. Energy Mater.*, 2020, **10**, 1902584.

115 M. H. Kumar, S. Dharani, W. L. Leong, P. P. Boix, R. R. Prabhakar, T. Baikie, C. Shi, H. Ding, R. Ramesh, M. Asta, M. Graetzel, S. G. Mhaisalkar and N. Mathews, *Adv. Mater.*, 2014, 7122–7127.

116 T. M. Koh, T. Krishnamoorthy, N. Yantara, C. Shi, W. L. Leong, P. P. Boix, A. C. Grimsdale, S. G. Mhaisalkar and N. Mathews, *J. Mater. Chem. A*, 2015, **3**, 14996–15000.

117 K. P. Marshall, M. Walker, R. I. Walton and R. A. Hatton, *Nat. Energy*, 2016, **1**, 16178.

118 X. Liu, Y. Wang, T. Wu, X. He, X. Meng, J. Barbaud, H. Chen, H. Segawa, X. Yang and L. Han, *Nat. Commun.*, 2020, **11**, 2678.

119 K. P. Marshall, R. I. Walton and R. A. Hatton, *J. Mater. Chem. A*, 2015, **3**, 11631–11640.

120 J. H. Heo, J. Kim, H. Kim, S. H. Moon, S. H. Im and K.-H. Hong, *J. Phys. Chem. Lett.*, 2018, **9**, 6024–6031.

121 F. Gu, S. Ye, Z. Zhao, H. Rao, Z. Liu, Z. Bian and C. Huang, *Sol. RRL*, 2018, **2**, 1800136.

122 T. Wang, Q. Tai, X. Guo, J. Cao, C.-K. Liu, N. Wang, D. Shen, Y. Zhu, C.-S. Lee and F. Yan, *ACS Energy Lett.*, 2020, **5**, 1741–1749.

123 J. Sanchez-Diaz, R. S. Sánchez, S. Masi, M. Krećmarová, A. O. Alvarez, E. M. Barea, J. Rodriguez-Romero, V. S. Chirvony, J. F. Sánchez-Royo, J. P. Martinez-Pastor and I. Mora-Seró, *Joule*, 2022, **6**(4), 861–883.

124 J. Sanchez-Diaz, R. S. Sánchez, S. Masi, M. Krećmarová, A. O. Alvarez, E. M. Barea, J. Rodriguez-Romero, V. S. Chirvony, J. F. Sánchez-Royo, J. P. Martinez-Pastor and I. Mora-Seró, *Joule*, 2022, **6**(4), 861–883.

125 M. H. Kumar, S. Dharani, W. L. Leong, P. P. Boix, R. R. Prabhakar, T. Baikie, C. Shi, H. Ding, R. Ramesh, M. Asta, M. Graetzel, S. G. Mhaisalkar and N. Mathews, *Adv. Mater.*, 2014, **26**, 7122–7127.

126 C. C. Stoumpos, L. Frazer, D. J. Clark, Y. S. Kim, S. H. Rhim, A. J. Freeman, J. B. Ketterson, J. I. Jang and M. G. Kanatzidis, *J. Am. Chem. Soc.*, 2015, **137**, 6804–6819.

127 X. Li, B. Li, J. Chang, B. Ding, S. Zheng, Y. Wu, J. Yang, G. Yang, X. Zhong and J. Wang, *ACS Appl. Energy Mater.*, 2018, **1**, 2709–2716.

128 M. Wang, P. Zeng, S. Bai, J. Gu, F. Li, Z. Yang and M. Liu, *Sol. RRL*, 2018, **2**, 1800217.

129 F. Li, C. Zhang, J.-H. Huang, H. Fan, H. Wang, P. Wang, C. Zhan, C.-M. Liu, X. Li, L.-M. Yang, Y. Song and K.-J. Jiang, *Angew. Chem., Int. Ed.*, 2019, **58**, 6688–6692.

130 E. Jokar, C.-H. Chien, C.-M. Tsai, A. Fathi and E. W.-G. Diau, *Adv. Mater.*, 2019, **31**, 1804835.

131 S. Shao, J. Liu, G. Portale, H. H. Fang, G. R. Blake, G. H. ten Brink, L. J. A. Koster and M. A. Loi, *Adv. Energy Mater.*, 2018, **8**(4), 1702019.

132 J. Qiu, Y. Xia, Y. Zheng, W. Hui, H. Gu, W. Yuan, H. Yu, L. Chao, T. Niu, Y. Yang, X. Gao, Y. Chen and W. Huang, *ACS Energy Lett.*, 2019, **4**, 1513–1520.

133 F. Hao, C. C. Stoumpos, D. H. Cao, R. P. H. Chang and M. G. Kanatzidis, *Nat. Photonics*, 2014, **8**, 489–494.

134 T. Yokoyama, D. H. Cao, C. C. Stoumpos, T.-B. Song, Y. Sato, S. Aramaki and M. G. Kanatzidis, *J. Phys. Chem. Lett.*, 2016, **7**, 776–782.

135 W. Liao, D. Zhao, Y. Yu, C. R. Grice, C. Wang, A. J. Cimaroli, P. Schulz, W. Meng, K. Zhu, R.-G. Xiong and Y. Yan, *Adv. Mater.*, 2016, **28**, 9333–9340.



136 Z. Zhao, F. Gu, Y. Li, W. Sun, S. Ye, H. Rao, Z. Liu, Z. Bian and C. Huang, *Adv. Sci.*, 2017, **4**, 1700204.

137 C. Ran, W. Gao, J. Li, J. Xi, L. Li, J. Dai, Y. Yang, X. Gao, H. Dong, B. Jiao, I. Spanopoulos, C. D. Malliakas, X. Hou, M. G. Kanatzidis and Z. Wu, *Joule*, 2019, **3**, 3072–3087.

138 M. M. Byranvand, T. Kim, S. Song, G. Kang, S. U. Ryu and T. Park, *Adv. Energy Mater.*, 2018, **8**, 1702235.

139 H. Taherianfard, G.-W. Kim, F. Ebadi, T. Abzieher, K. Choi, U. W. Paetzold, B. Richards, A. Alrhman Eliwi, F. Tajabadi, N. Taghavinia and M. Malekshahi Byranvand, *ACS Appl. Mater. Interfaces*, 2019, **11**, 44802–44810.

140 X. Jiang, H. Li, Q. Zhou, Q. Wei, M. Wei, L. Jiang, Z. Wang, Z. Peng, F. Wang, Z. Zang, K. Xu, Y. Hou, S. Teale, W. Zhou, R. Si, X. Gao, E. H. Sargent and Z. Ning, *J. Am. Chem. Soc.*, 2021, **143**, 10970–10976.

141 J. Zhou, M. Hao, Y. Zhang, X. Ma, J. Dong, F. Lu, J. Wang, N. Wang and Y. Zhou, *Matter*, 2022, **5**, 683–693.

142 M. Loi, A. Villani, F. Paciolla, G. Mulè and C. Paciolla, *Antioxidants*, 2021, **10**.

143 C. Alonso, M. M. Byranvand, S. Essig and M. Saliba, *J. Mater. Chem. A*, 2022, DOI: [10.1039/D2TA01135B](https://doi.org/10.1039/D2TA01135B).

144 T.-L. Wu, M.-J. Huang, C.-C. Lin, P.-Y. Huang, T.-Y. Chou, R.-W. Chen-Cheng, H.-W. Lin, R.-S. Liu and C.-H. Cheng, *Nat. Photonics*, 2018, **12**, 235–240.

145 D. Yang, G. Zhang, R. Lai, Y. Cheng, Y. Lian, M. Rao, D. Huo, D. Lan, B. Zhao and D. Di, *Nat. Commun.*, 2021, **12**, 4295.

146 K. Masaoka, Y. Nishida and M. Sugawara, *Opt. Express*, 2014, **22**, 19069–19077.

147 J. Lu, X. Guan, Y. Li, K. Lin, W. Feng, Y. Zhao, C. Yan, M. Li, Y. Shen, X. Qin and Z. Wei, *Adv. Mater.*, 2021, **33**, 2104414.

148 J. Lu, X. Guan, Y. Li, K. Lin, W. Feng, Y. Zhao, C. Yan, M. Li, Y. Shen, X. Qin and Z. Wei, *Adv. Mater.*, 2021, **33**, 2104414.

149 H. Zhang, Z. Yang, M. Zhou, L. Zhao, T. Jiang, H. Yang, X. Yu, J. Qiu, Y. Yang and X. Xu, *Adv. Mater.*, 2021, **33**, 2102529.

150 Y. C. Kim, K. H. Kim, D.-Y. Son, D.-N. Jeong, J.-Y. Seo, Y. S. Choi, I. T. Han, S. Y. Lee and N.-G. Park, *Nature*, 2017, **550**, 87–91.

151 L. Pan, S. Shrestha, N. Taylor, W. Nie and L. R. Cao, *Nat. Commun.*, 2021, **12**, 5258.

152 M. D. Birowosuto, D. Cortecchia, W. Drozdowski, K. Brylew, W. Lachmanski, A. Bruno and C. Soci, *Sci. Rep.*, 2016, **6**, 1–10.

153 M. Konstantakou and T. Stergiopoulos, *J. Mater. Chem. A*, 2017, **5**, 11518–11549.

